Pacific Northwest
NATIONAL LABORATORY

PNNL-39822

High Temperature Mechanical Performance of DED Fe-Based Alloys for Reactor Environments

September 2026

Subhashish Meher
Jens Darsell
Jon Lapeyre
Francelia Sanchez
Mohan Nartu
Isabella van Rooyen

M3MT-26PN0201052

U.S. DEPARTMENT of ENERGY

Prepared for the U.S. Department of Energy
under Contract DE-AC05-76RL01830

DISCLAIMER

This report was prepared as an account of work sponsored by an agency of the United States Government. Neither the United States Government nor any agency thereof, nor Battelle Memorial Institute, nor any of their employees, makes **any warranty, express or implied, or assumes any legal liability or responsibility for the accuracy, completeness, or usefulness of any information, apparatus, product, or process disclosed, or represents that its use would not infringe privately owned rights**. Reference herein to any specific commercial product, process, or service by trade name, trademark, manufacturer, or otherwise does not necessarily constitute or imply its endorsement, recommendation, or favoring by the United States Government or any agency thereof, or Battelle Memorial Institute. The views and opinions of authors expressed herein do not necessarily state or reflect those of the United States Government or any agency thereof.

PACIFIC NORTHWEST NATIONAL LABORATORY
operated by
BATTELLE
for the
UNITED STATES DEPARTMENT OF ENERGY
under Contract DE-AC05-76RL01830

Printed in the United States of America

Available to DOE and DOE contractors from
the Office of Scientific and Technical Information,
P.O. Box 62, Oak Ridge, TN 37831-0062
www.osti.gov
ph: (865) 576-8401
fax: (865) 576-5728
email: reports@osti.gov

Available to the public from the National Technical Information Service
5301 Shawnee Rd., Alexandria, VA 22312
ph: (800) 553-NTIS (6847)
or (703) 605-6000
email: info@ntis.gov
Online ordering: http://www.ntis.gov

PNNL-39822

High Temperature Mechanical Performance of DED Fe-Based Alloys for Reactor Environments

September 2026

Subhashish Meher
Jens Darsell
Jon Lapeyre
Francelia Sanchez
Mohan Nartu
Isabella van Rooyen

M3MT-26PN0201052

Prepared for
the U.S. Department of Energy
under Contract DE-AC05-76RL01830

Pacific Northwest National Laboratory
Richland, Washington 99354

Summary

Laser powder directed energy deposition (LP-DED) is an attractive route for fabricating and repairing high-temperature structural components in advanced nuclear energy systems. However, the rapid-solidification cellular substructure, columnar grain morphology, crystallographic texture, and non-equilibrium solute distributions intrinsic to the process complicate both mechanical qualification and the transfer of conventional heat-treatment practice from wrought product forms. In this work, LP-DED Alloy 709 (an advanced austenitic stainless steel) and LP-DED Grade 92 (a 9Cr tempered-martensitic creep-resistant steel) were examined across a matrix of post-deposition heat treatments to establish the relationship between processing, microstructure and elevated-temperature mechanical response.

Alloy 709 was evaluated as-deposited (AD), solution annealed at 1150°C for 1 h (SA), precipitation treated at 775°C for 10 hours (h) (PT), and solution annealed plus precipitation treated (SA+PT). Grade 92 was evaluated as-deposited, tempered at 775°C for 45 min (T), normalized at 1070°C for 15 min (N), and normalized plus tempered (N+T). Tensile tests were performed at room temperature and 550°C on horizontally and vertically extracted specimens, creep tests were conducted against matched wrought benchmarks, pre-test X-ray computed tomography established the internal defect population, and precipitate chemistry was resolved by atom probe tomography (APT). Main findings describe as follows:

- In Alloy 709, the AD condition exhibited the highest strength while retaining more than 30% elongation, attributed to the retained solidification cell network, high dislocation density, and cell-boundary solute segregation. SA gave the lowest strength but the greatest tensile ductility, PT raised flow stress while restricting elongation, and SA+PT provided the most balanced response. Property-retention analysis at 550°C showed that conditions preserving elements of the deposition substructure retained yield strength most effectively, indicating that complete homogenization is not automatically optimal for elevated-temperature strength.
- The Alloy 709 creep results provided the clearest differentiation. The AD condition accumulated very little strain, remaining essentially undeformed beyond 1500-1800 h and substantially outlasting the wrought reference; however, these tests remain in progress and have produced no measurable creep elongation, so the creep ductility and damage tolerance of AD are unproven. Among the ruptured conditions, SA failed after 180 h with only 9 % elongation and 8.6 % reduction in area (RA), whereas SA+PT failed after 350 h with 33 % elongation and 30 % RA, doubling rupture life while more than tripling creep ductility and approaching wrought-like behavior. Macroscopic fracture appearance and fractography corroborated this, showing a progression from boundary-dominated, low-ductility failure in SA, through mixed-mode fracture in SA+PT, to fully transgranular ductile cavitation in wrought material. SA+PT is therefore identified as the best-performing DED condition evaluated.
- The Alloy 709 APT analysis of the PT condition resolved discrete Nb- and C-rich MX-type precipitates[1] within a chemically homogeneous austenite matrix, with abrupt 1-2 nm interfaces and no adjacent Cr depletion, indicating that precipitation does not sensitize the matrix. This intragranular dispersion provides the direct microstructural explanation for the superior creep life and ductility of SA+PT, redistributing strain into grain interiors and

[1] MX precipitates are nanoscale carbonitride particles found in advanced ferritic/martensitic and micro-alloyed steels where M represents a transition metal (like titanium, tantalum, vanadium, or niobium) and X represents carbon, nitrogen, or both.

delaying cavity coalescence at boundaries. X-ray computed tomography showed that SA and SA+PT contain comparable porosity, unchanged by heat treatment, confirming that the ductility difference originates from the precipitate and matrix state rather than from defects; the porosity itself accounts for the off-center creep fractures and residual build anisotropy.

In Grade 92, the tensile matrix was completed with the N and N+T conditions. Strength was governed by the state of tempered martensite and by carbide/MX precipitation, with AD strongest but insufficiently ductile, particularly at 550°C, and N showing the highest property retention. APT of N+T resolved a fine dispersion of Nb- and V-rich MX carbonitrides with homogeneous Cr, W and Mo distributions, implying that the W contribution operates principally through the matrix rather than through partitioning into the MX phase. Since the Alloy 709 results demonstrate that a stable intragranular MX dispersion is the source of creep ductility and life, N+T remains the microstructurally preferred condition despite its modest tensile ranking; the planned creep matrix will resolve this.

Finally, a neutron-irradiation matrix of 16 Alloy 709 specimens at 500 and 600°C to 2 and 10 displacements per atom was defined, with emphasis on SA+PT. The results are interpreted within a framework in which the LP-DED cell network is treated as an engineerable but metastable strengthening feature rather than solely as a defect, and in which creep ductility, not creep rate alone, is adopted as the primary measure of performance.

Acknowledgments

The research presented herein was supported by the Advanced Materials and Manufacturing Technology program of the U.S. Department of Energy (DOE), Office of Nuclear Energy. Pacific Northwest National Laboratory (PNNL) is a multiprogram national laboratory operated for the Department of Energy by Battelle Memorial Institute under Contract No. DE-AC05-76RL01830. We would like to acknowledge Prof. Xiaoyuan Lou and students John Snitzer and Qianwen Zhang from Purdue University for the laser directed energy deposition of Alloy 709 and Grade 92 steels on behalf of PNNL. We also acknowledge the contributions of the following PNNL staff: Dave Olson (extracting tensile specimens from fabricated blocks), Mark Rhodes (assistance with the heat treatments), Rob Seffens (tensile testing), and the entire metallography team at the PNNL Materials Science and Technology Laboratory (sample preparation). The language in this document was edited using OpenAI (gpt-5.6-sol) to improve grammar and clarity. Initial drafts were created by the author, and all final content was reviewed for accuracy.

Acronyms and Abbreviations

AD	as-deposited
AMMT	Advanced Materials and Manufacturing Technologies
APT	atom probe tomography
ASTM	ASTM International (formerly American Society for Testing and Materials)
DED	directed energy deposition
dpa	displacements per atom
EL	elongation
FY	fiscal year
G-91	Grade 91 steel (9Cr–1Mo ferritic-martensitic steel)
G-92	Grade 92 steel (9Cr–0.5Mo–1.8W ferritic-martensitic steel)
h	hour
H	horizontal (build orientation; loading axis perpendicular to build direction)
LP-DED	laser powder directed energy deposition
LPBF	laser powder bed fusion
MX	metal–interstitial carbonitride precipitate (M = Nb, V; X = C, N)
N	normalized
N+T	normalized plus tempered
PT	precipitation treatment/precipitation treated
RA	reduction in area
RT	room temperature
SA	solution annealing/solution annealed
SA+PT	solution annealed plus precipitation treated
SEM	scanning electron microscopy
SSJ-2	miniature (subsize) tensile specimen geometry used for irradiation testing
T	tempered
TEM	transmission electron microscopy
UTS	ultimate tensile strength
V	vertical (build orientation; loading axis parallel to build direction)
XCT	X-ray computed tomography
YS	yield strength

Contents

Summary ii
Acknowledgments iv
Acronyms and Abbreviations v
1.0 Introduction 1
1.1 Background 1
1.2 Importance of LP-DED for Nuclear Applications 1
1.3 Microstructural Consequences of the LP-DED Thermal History 2
1.4 Alloys and Heat-Treatment Matrices 3
1.5 Objectives 3
2.0 Experimental 4
2.1 Material Fabrication 4
2.2 Post-Deposition Heat Treatments 5
2.3 Specimen Extraction and Orientation Convention 5
2.4 Tensile Testing 6
2.5 Creep Testing 6
2.6 Electron Microscopy 6
2.7 Atom Probe Tomography 6
3.0 Results 7
3.1 Tensile Response of LP-DED Alloy 709 7
3.2 Creep Response of LP-DED Alloy 709 9
3.3 Tensile Response of LP-DED Grade 92 19
3.4 Creep Benchmarking of LP-DED Grade 91 and Grade 92 21
3.5 Atom Probe Tomography of Normalized-and-Tempered Grade 92 23
4.0 Neutron Irradiation Plan of DED A709 26
5.0 Discussion 28
5.1 Role of the As-Deposited Substructure 28
5.2 Effect of Heat Treatment 28
5.3 Interpretation of the Creep Results 28
5.4 Mechanistic Basis for the SA+PT Advantage 29
5.5 Selection of an Optimum Condition 29
5.6 Implications for the Irradiation Study 30
6.0 Conclusions 31
6.1 Tensile Behavior of LP-DED Alloy 709 31
6.2 Creep Behavior and the Selection of SA+PT 31
6.3 Mechanistic Basis 31
6.4 Process-Induced Defects 32
6.5 LP-DED Grade 92 32

6.6 Outlook 32
7.0 Path Forward 33
7.1 Completion and Reconciliation of the Existing Dataset 33
7.2 Benchmarking Objective 33
7.3 Microstructure–Thermodynamics Linkage 33
7.4 Irradiation Program 34
8.0 Publications and Presentations 35
8.1 Publications 35
8.2 Conferences 35
8.3 Milestone Reports 35
8.4 AMMT Annual Program Review Meeting Presentations 35
9.0 References 36

Figures

Figure 1. Geometry, Build Layout, and Fabricated Samples of the Tensile Specimens (left) and Threaded Creep Specimens (right). Specimen Dimensions, Build-Platform Arrangement, and Representative As-Fabricated Parts are included. 4

Figure 2. Representative Engineering Stress–Strain Curves for DED-Fabricated Alloy 709, Benchmarked Against Wrought Materials. The results illustrate the effects of post-build heat treatment and horizontal (H) and vertical (V) specimen orientations on tensile strength, strain hardening, and ductility. 7

Figure 3. Comparison of the Measured Responses of DED-Fabricated A709 Steel Under Different Processing Conditions. Red ellipses identify the selected conditions, while the inset shows a representative SEM micrograph of the corresponding microstructure. 8

Figure 4. Fractographs Showing Low- and High-Magnification Views of the Tensile Fracture Surfaces. The images reveal a predominantly ductile fracture characterized by micro-void nucleation, growth, and coalescence, along with localized pores and processing-related defects. 9

Figure 5. Creep Properties and Post-Creep Fractography of DED-Fabricated A709 Steel Under Different Heat-Treatment, Temperature, and Applied-Stress Conditions. The creep elongation–time curves compare DED and wrought A709 tested at 650-750°C and 140–311 MPa, illustrating the effects of processing condition and heat treatment on creep deformation, rupture life, and fracture behavior. 10

Figure 6 Photographs of Failed Creep Specimens of Wrought and DED-Fabricated A709 Steel After Testing Under Various Temperature–Stress Conditions. The specimens show differences in creep deformation, necking, and fracture location as a function of material condition and heat treatment, including stress annealing (SA) and stress annealing plus post-treatment (SA+PT). Scale bar: 25.4 mm. 13

Figure 7 X-Ray Computed Tomography (XCT) Reconstructions of the Gauge Sections of Pre-Creep Tensile/Creep Specimens. (a, d) Wrought A709, (b, e) LP-DED A709 in the solution-annealed (SA) condition, and (c, f) LP-DED A709 in the solution-annealed plus precipitation-treated (SA+PT) condition. Top row (a–c) shows representative transverse (X–Y) cross-sectional slices; bottom row (d–f) shows longitudinal (Y–Z) slices along the loading/build direction. Insets in (a) and (d) indicate the interrogated gauge region relative to the specimen geometry. Dark contrast features correspond to internal porosity and lack-of-fusion defects. 15

Figure 8. SEM fractographs of Creep-Ruptured A709 Specimens Tested at 650°C/275 MPa, Shown at Low Magnification (left) and High Magnification (right). (a) Wrought A709, (b) LP-DED A709 in the solution-annealed (SA) condition, and (c) LP-DED A709 in the solution-annealed plus precipitation-treated (SA+PT) condition. 16

Figure 9. Atom Probe Tomography (APT) Analysis of LP-DED A709 in the As-Heat-Treated Precipitation-Treated (PT) Condition, Prior to Mechanical Testing. (a) Three-dimensional reconstruction of the APT tip showing the spatial distribution of the matrix and a solute-enriched feature

(Nb atoms in blue). (b) Individual elemental atom maps for Fe, Cr, Ni, Mo, Si, C, Nb, S and N extracted from the same reconstruction, together with a TEM image of the corresponding needle geometry..... 17

Figure 10. Quantitative Atom Probe Tomography (APT) Analysis of LP-DED A709 in the As-Heat-Treated Precipitation-Treated (PT) condition, Prior to Mechanical Testing. (a) Iso-concentration surface delineating the precipitate/matrix interface within the reconstructed volume (Fe atoms shown in red). (b, c) Proximity histograms (proxigrams) computed normal to the iso-surface showing the concentration profiles of (b) the major alloying and interstitial species (Ni, Fe, Cr, Si, C, Nb) and (c) the minor species (Mo, N, S, P). 18

Figure 11. Representative Engineering Stress–Strain Curves for LP-DED-Fabricated Grade 92 (G-92) Steel Tested at (a) Room Temperature and (b) Elevated Temperature. The figures compare the as-deposited (AD), tempered, normalized (N), and normalized-plus-tempered (N+T) conditions for horizontal (H) and vertical (V) build orientations..... 19

Figure 12. Retention of Tensile Properties at 550°C Relative to Room Temperature for LP-DED Grade 92 Steel. (a) Yield strength retention ratio (YS-550°C/YS-RT) and (b) elongation retention ratio (EL-550°C/EL-RT) 20

Figure 13. SEM Fractographs of Tensile-Tested LP-DED Grade 92 Steel at Low And High Magnification. (a, b) Normalized-plus-tempered (N+T) tested at room temperature, (c, d) normalized (N) tested at room temperature, (e, f) N+T tested at 550°C, and (g, h) N tested at 550°C. 21

Figure 14. Photographs of Machined, Threaded-End Creep Specimens Prepared from LP-DED-Fabricated Grade 92 (G-92, left) and Grade 91 (G-91, right) Steels 22

Figure 15. Atom Probe Tomography (APT) Analysis of LP-DED Grade 92 Steel in the Normalized-Plus-Tempered (N+T) Condition. (a) Three-dimensional reconstruction showing iso-concentration surfaces (blue) delineating multiple nanoscale precipitates distributed within the tempered martensitic matrix; scale bar 10 nm. (b) Corresponding elemental atom maps for Fe, C, Nb, V, Si, Mn, W, Cr, Mo, and N extracted from the same volume; scale bar 20 nm. 23

Figure 16. Quantitative APT Analysis Of Precipitates in LP-DED Grade 92 (N+T condition). (a) Nb atom map showing the precipitate distribution within the analyzed volume; scale bar 70 nm. (b, c) Proximity histograms across the precipitate/matrix interface for (b) major species (Fe, Cr, V, Si, C, Nb) and (c) minor species (Mn, Mo, W, N); negative distances correspond to the matrix, positive distances to the precipitate. (d, e) Location and corresponding concentration/ion-count profile of a one-dimensional line scan across a single precipitate. 24

Figure 17. Neutron Irradiation Matrix for LP-DED-Fabricated A709 Planned at the High-Flux Isotope Reactor, Oak Ridge National Laboratory. SSJ-2 miniature tensile specimens (inset, shown against a centimeter scale) will be irradiated in the as-deposited (AD), solution-annealed (SA), and solution-annealed plus precipitation-treated (SA+PT) conditions at 500 and 600°C to nominal doses of 2 and 10 displacements per atom (dpa), with two specimens per condition for a total of 16 specimens..... 26

Tables

Table 1. Heat Treatment for A709 Steel 5
Table 2. Heat Treatment for G-92 Steel 5
Table 3. Summary of Creep-Test Conditions and Results for Wrought and Vertically Built DED A709 Steel in the As-Deposited (AD), Stress-Annealed (SA), and Stress-Annealed Plus Post-Treated (SA+PT) Conditions. An asterisk indicates an ongoing test duration at the time of reporting. 11
Table 4. Planned Creep Test Matrix for LP-DED-Fabricated Grade 91 and Grade 92 Steels. The table shows selected temperature–stress combinations for the as-deposited (AD), normalized (N), and normalized-plus-tempered (N+T) conditions. 23

1.0 Introduction

1.1 Background

Advanced fission reactors require structural alloys capable of sustaining load for tens of thousands of hours at temperatures where diffusional processes are active. Under these conditions the limiting damage mechanisms extend well beyond plastic instability, encompassing creep deformation and cavitation, precipitate coarsening, phase instability, creep–fatigue interaction, and for near-core components, irradiation hardening and radiation-induced microstructural evolution. Therefore, alloy qualification requires both an extensive property database and a mechanistic understanding of why the microstructure remains stable.

1.2 Importance of LP-DED for Nuclear Applications

Sustained research on laser powder directed energy deposition (LP-DED) is essential for establishing additive manufacturing pathways for large, high-value nuclear components that cannot be efficiently produced by laser powder bed fusion (LPBF) [1]. The LP-DED process combines relatively high deposition rates, flexible build envelopes, localized material placement, and the ability to add material to existing components. These capabilities make it especially attractive for near-net-shape fabrication, repair, surface modification, and functional grading, and they can substantially reduce material waste and lead time for advanced Fe-based alloys for which conventional manufacture may require multiple forging, casting, machining, and joining operations. Nuclear deployment, however, requires a defensible understanding of process variability, anisotropy, defects, residual stresses, heat-treatment response and long-term degradation, which in turn requires the processing–microstructure–property linkages that Advanced Materials and Manufacturing Technologies (AMMT) program is intended to establish.

The process is relevant across light-water reactors, sodium-cooled fast reactors, molten-salt reactors, high-temperature gas-cooled reactors, and microreactors. Candidate applications include valve bodies and internals, pump housings and impellers, flow distributors, support structures, nozzles, transition pieces, heat-exchanger headers and manifolds, piping features, shielding structures, and other complex or low-production-volume components. The LP-DED process may also support fabrication or restoration of wear- and corrosion-resistant surfaces on valve seats, shafts, and pump components. For advanced reactors specifically, it could enable compact heat-transfer and flow-control components, compositionally graded transitions, and localized deposition of materials selected for creep, corrosion, wear, or irradiation resistance. Repair and refurbishment are potentially the highest-value near-term applications, because LP-DED can restore geometry or apply protective material without replacing an entire component. Actual deployment will nevertheless depend on component-specific design, code, inspection, environmental, and qualification requirements, particularly for pressure-boundary or safety-related applications. These considerations underpin the programmatic interest in LP-DED Alloy 709 and Grade 92 within the AMMT program.

1.3 Microstructural Consequences of the LP-DED Thermal History

The central materials challenge is that the thermal history of LP-DED differs substantially from that of both hot-worked, heat-treated wrought plate, and LPBF. In LP-DED, each material volume solidifies at cooling rates of approximately 10^3–10^6 K s^{-1} and is subsequently reheated by adjacent tracks and overlying layers [2]. Although LPBF produces many of the same rapid-solidification features, its smaller melt pools and generally higher cooling rates usually generate finer cellular structures and steeper local thermal gradients. By contrast, the larger melt pools, greater heat accumulation, and longer high-temperature dwell times characteristic of LP-DED promote coarser cells and grains, more extensive intrinsic thermal cycling, and stronger spatial variation in recovery, precipitation, and phase transformation.

Both processes commonly produce columnar grains aligned with the principal heat-flow direction, associated crystallographic texture, solute-enriched cellular or dendritic boundaries, elevated dislocation densities, and residual stresses. These features are often finer and more strongly retained in the as-built LPBF condition, whereas the repeated thermal exposure experienced during LP-DED can partially recover the dislocation structure or initiate precipitation and transformation during deposition. Consequently, LP-DED microstructures may vary appreciably with build height and with position relative to track and layer boundaries. Lack-of-fusion defects and gas porosity can occur in both processes, although their morphology and distribution reflect the different powder-delivery and melt-pool geometries. Because such defects are geometric discontinuities rather than matrix-scale microstructural features, they are not removed by conventional heat treatment.

Whether these deposition-induced features are beneficial cannot be determined from strength alone. A fine cellular network enriched in slowly partitioning solutes and decorated with dislocations can increase yield strength, impede thermally activated dislocation climb, and substantially reduce the minimum creep rate [3]. This strengthening is often especially pronounced in LPBF because of its finer solidification substructure; however, the somewhat coarser and partially thermally evolved LP-DED network may offer greater stability, depending on alloy chemistry and deposition history. In either process, the cellular network remains thermodynamically metastable and may recover or dissolve during prolonged high-temperature exposure, making any associated strengthening transient. Its continuous chemical heterogeneity also may provide preferential sites or paths for cavity nucleation and growth [4].

Critically, a microstructure that suppresses creep deformation is not necessarily capable of accommodating creep strain. Damage tolerance depends on the latter capacity, expressed through creep elongation and reduction in area (RA), which also provides a deformation-based indication of remaining life [5]. The question addressed here is therefore not simply whether the LP-DED microstructure should be homogenized to resemble wrought material or whether the finer as-built structure typical of LPBF should be reproduced but which deposition-induced features should be retained, stabilized or transformed. The corresponding criterion is whether the resulting condition fails through a ductile, deformation-controlled process or through localized, boundary-dominated damage.

1.4 Alloys and Heat-Treatment Matrices

Alloy 709 is an advanced austenitic stainless steel in which creep strength derives from solid-solution strengthening, boundary stabilization, and controlled dispersion of nanoscale precipitates [6]. Applying wrought heat-treatment logic to LP-DED material is not straightforward, since the as-deposited (AD) matrix is not a homogeneous solid solution but a cellular arrangement of solute-lean interiors and solute-enriched boundaries, with a far higher dislocation density and columnar grains. Nucleation-site density, local supersaturation, and diffusion distances therefore all differ. The matrix used here, AD, solution annealed (SA, 1150°C/1 h), precipitation treated (PT, 775°C/10 h), and combined SA+PT, separates these effects [7-10]. Comparison of SA with SA+PT is the most informative pair, testing directly whether an engineered precipitate dispersion can substitute mechanically for the metastable deposition substructure that solution annealing removes. Because the identity and interfacial chemistry of that dispersion cannot be resolved by conventional methods at the relevant length scale, atom probe tomography is used to establish precipitate composition and matrix solute levels directly.

Grade 92 is a 9Cr ferritic-martensitic steel whose properties depend on a transformation-derived hierarchy of prior-austenite grains, packets, blocks, and martensite laths, stabilized by Cr-rich boundary carbides and a fine dispersion of Nb- and V-rich MX carbonitrides, with additional solid-solution strengthening from W and Mo [11]. Because this architecture arises from transformation, normalizing is not optional as solution annealing might be for an austenitic alloy. LP-DED Grade 92 is especially demanding because each deposited volume may undergo repeated partial austenitization and tempering, producing spatial non-uniformity superimposed on cellular segregation and columnar morphology. The matrix, AD, tempered only (T, 775°C/45 min), normalized only (N, 1070°C/15 min) and normalized plus tempered (N+T), separates re-austenitization from tempering [12]. A specific concern, tested rather than assumed, is that the condition with the best short-term tensile properties may not contain the stable dispersion required for long-term creep performance.

1.5 Objectives

This LP-DED study is structured as a coordinated program to be completed by the end of fiscal year (FY) 2027. First, the tensile response of LP-DED Alloy 709 and Grade 92 will be established at room temperature (RT) and 550°C across systematic heat-treatment matrices and in two build orientations. Second, creep performance will be benchmarked against wrought material tested under identical conditions, with emphasis on creep ductility and RA, as well as rupture life. Third, process-induced defect populations will be characterized by X-ray computed tomography to distinguish their contributions to anisotropy and damage localization from those of the matrix microstructure. Fourth, atom probe tomography will be used to determine the compositions of precipitates formed during each heat treatment and relate them to the measured creep behavior. Finally, an irradiation matrix will be defined and implemented to evaluate the stability of the most promising conditions under combined thermal exposure and displacement damage. Integration of the mechanical-testing, defect-characterization, precipitation, and irradiation results, and identification of the most promising processing conditions, is planned for completion by the end of FY 2027.

2.0 Experimental

2.1 Material Fabrication

Tensile specimens of LP-DED A709 and G-92 were fabricated using process parameters optimized during preliminary development studies in FY 2024. A709 was deposited at 400 W laser power and 700 mm/min scan velocity, and G-92 at 500 W and 700 mm/min, with hatch spacing, layer thickness, and powder feed rate held constant throughout each build. These conditions were selected to produce high-density, defect-free deposits suitable for subsequent heat treatment and mechanical property evaluation. Figure 1 shows the resulting A709 and G-92 test blocks.

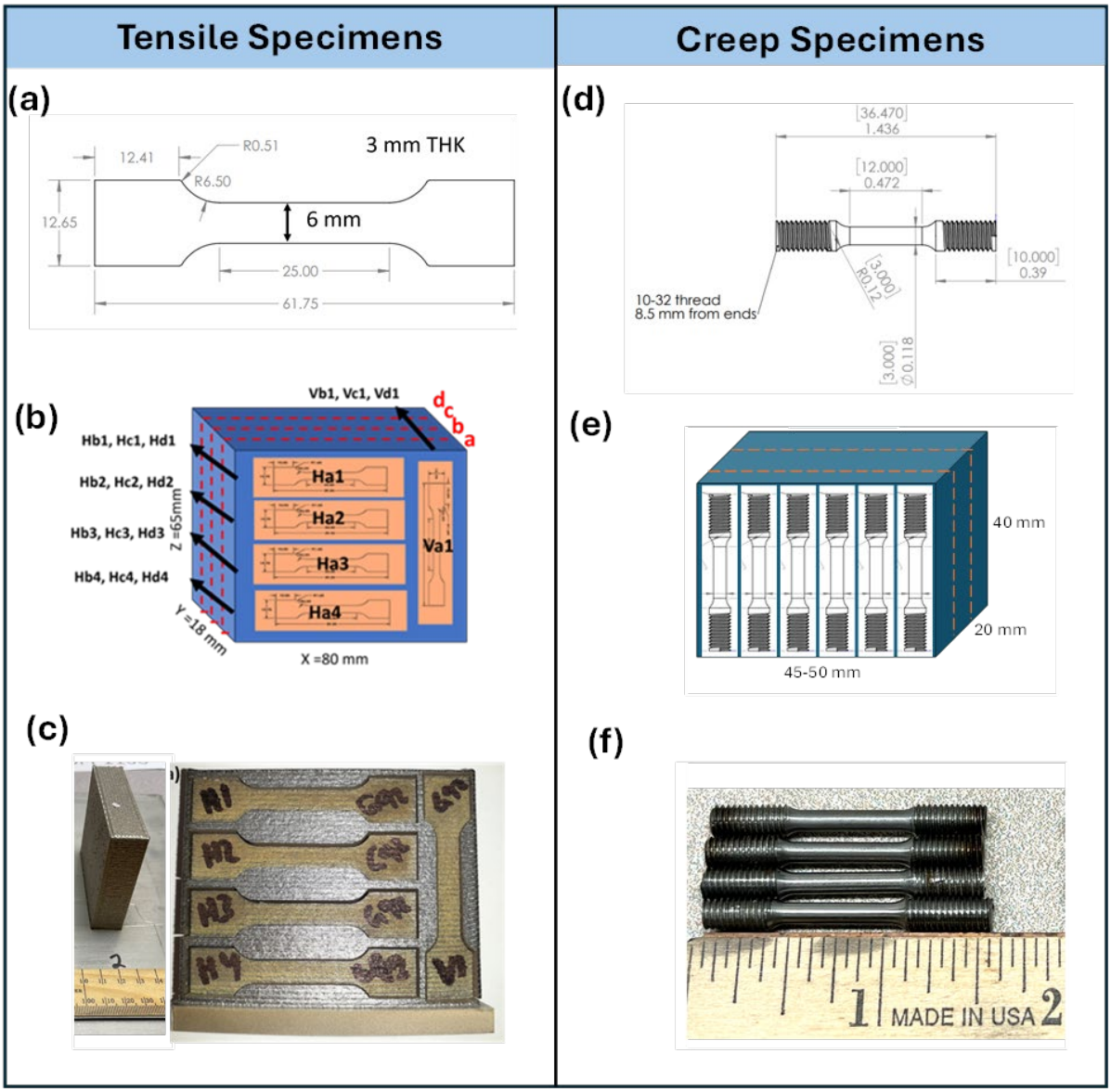


Figure 1. Geometry, Build Layout, and Fabricated Samples of the Tensile Specimens (left) and Threaded Creep Specimens (right). Specimen Dimensions, Build-Platform Arrangement, and Representative As-Fabricated Parts are included.

2.2 Post-Deposition Heat Treatments

Following deposition, A709 and G-92 specimens were heat treated according to the schedules given in Table 1 and Table 2, respectively. All treatments were carried out in a Vulcan model 3-550 and Thermolyne model 48025 furnaces, with water quenching applied after each step.

Table 1. Heat Treatment for A709 Steel

Heat Treatment	Temperature and Time	Quenching Medium
Solution Annealing (SA)	1150°C/1 h	Water Quench
Precipitation Treatment (PT)	775°C/10 h	Water Quench
SA+PT	1150°C/1 hour + 775°C/10 hours	Water Quench

Table 2. Heat Treatment for G-92 Steel

Heat Treatment	Temperature and Time	Quenching Medium
Normalizing	1070°C/15 minutes	Water Quench
Tempering	775°C/45 min	Water Quench
Normalizing + Tempering (Dual Step)	1070°C/15 min + 775°C/45 minutes	Water Quench

2.3 Specimen Extraction and Orientation Convention

Figure 1 summarizes the specimen geometries, extraction layouts, and as-machined parts for both test types. Tensile specimens [Figure 1(a)] were flat, dog-bone coupons of 3 mm thickness with a 6 mm wide, 25 mm long reduced gauge section, an overall length of 61.75 mm and fillet radii of 6.50 and 0.51 mm. The extraction layout in Figure 1(b) shows how these coupons were located within an 80 × 18 × 65 mm deposited block: horizontal specimens were extracted along the build height, while vertical specimens were extracted with their loading axis parallel to the build direction. This arrangement allowed both orientations to be obtained from a common deposit, so that any difference in tensile response could be attributed to orientation rather than to build-to-build variation. Figure 1(c) shows a representative AD block together with the sectioned and marked tensile blanks prior to final machining.

Creep specimens [Figure 1(d)] were threaded, round bars with a 3.0 mm diameter, 12.0 mm long gauge section, 10-32 threads terminating 8.5 mm from each end, and an overall length of 36.47 mm; the shoulder radius was 0.12 mm. The build layout in Figure 1(e) indicates that such specimens were extracted in parallel from a 45–50 × 20 × 40 mm block, again with the specimen axis defined relative to the build direction. Figure 1(f) shows the finished creep bars against a scale, confirming good dimensional uniformity and the absence of visible machining damage or surface defects, both of which are important for minimizing scatter in rupture-life measurements.

2.4 Tensile Testing

Uniaxial tensile testing was performed using an MTS Systems Corporation 10-kip (45 kN) servo-hydraulic testing machine with Instron Bluehill 2 software and an Epsilon One noncontact optical extensometer. The extensometer uses telecentric lenses for precise strain measurements up to a gauge length of 50 mm with a resolution of ±0.1 µm, maintaining accuracy despite the out-of-plane movement of the specimen.

The configuration included an Applied Test Systems clamshell furnace with a 150 mm heating zone for elevated temperature testing and hydraulically actuated shoulder-loaded grips with ball-and-socket articulation for proper axial alignment. The Bluehill 2 software provided automated test control, real-time data acquisition, and systematic compilation of engineering stress–strain data throughout each test cycle.

2.5 Creep Testing

Creep tests were conducted in accordance with ASTM E139 and the applicable provisions of ASTM E8 using a Satec Systems Inc. creep frame (formerly SSi; now part of Instron's IPG division). A high-temperature furnace supplied by Applied Test Systems was mounted around the wedge grips to enclose the entire specimen.

2.6 Electron Microscopy

An FEI APREO 2 scanning electron microscope (SEM) equipped with energy-dispersive X-ray spectrometry was used to examine the cross-sectional phase constituents, microstructures, and compositions of A709 and G-92 samples.

2.7 Atom Probe Tomography

Atom probe tomography (APT) was used to resolve the nanoscale chemistry of the strengthening precipitates and surrounding matrix in precipitation-treated Alloy 709 and normalized-and-tempered Grade 92. Each reconstruction was analyzed by three-dimensional elemental mapping, iso-concentration-surface delineation of the precipitate/matrix interface, and proximity (proxigram) composition profiles across that interface. APT was performed using a CAMECA local electrode atom probe (LEAP) 6000 XR operated in voltage-pulsing mode. A pulse fraction of 0.20 was applied at a pulse frequency of 200 kHz, with the detection rate held at a target of 0.005 ions per pulse and the specimen temperature maintained at 40 K throughout acquisition. Datasets were reconstructed and analyzed using CAMECA Interactive Visualization and Analysis Software (IVAS, version 6.3).

3.0 Results

3.1 Tensile Response of LP-DED Alloy 709

Figure 2 compares representative engineering stress–strain curves for LP-DED A709 in the AD and post-build, heat-treated conditions with wrought Alloy 709. Tensile testing of the AD and SA+PT conditions was carried out in FY 2025; the SA and PT conditions were completed in FY 2026, thereby completing the tensile matrix for LP-DED Alloy 709 across all heat-treatment conditions and both build orientations.

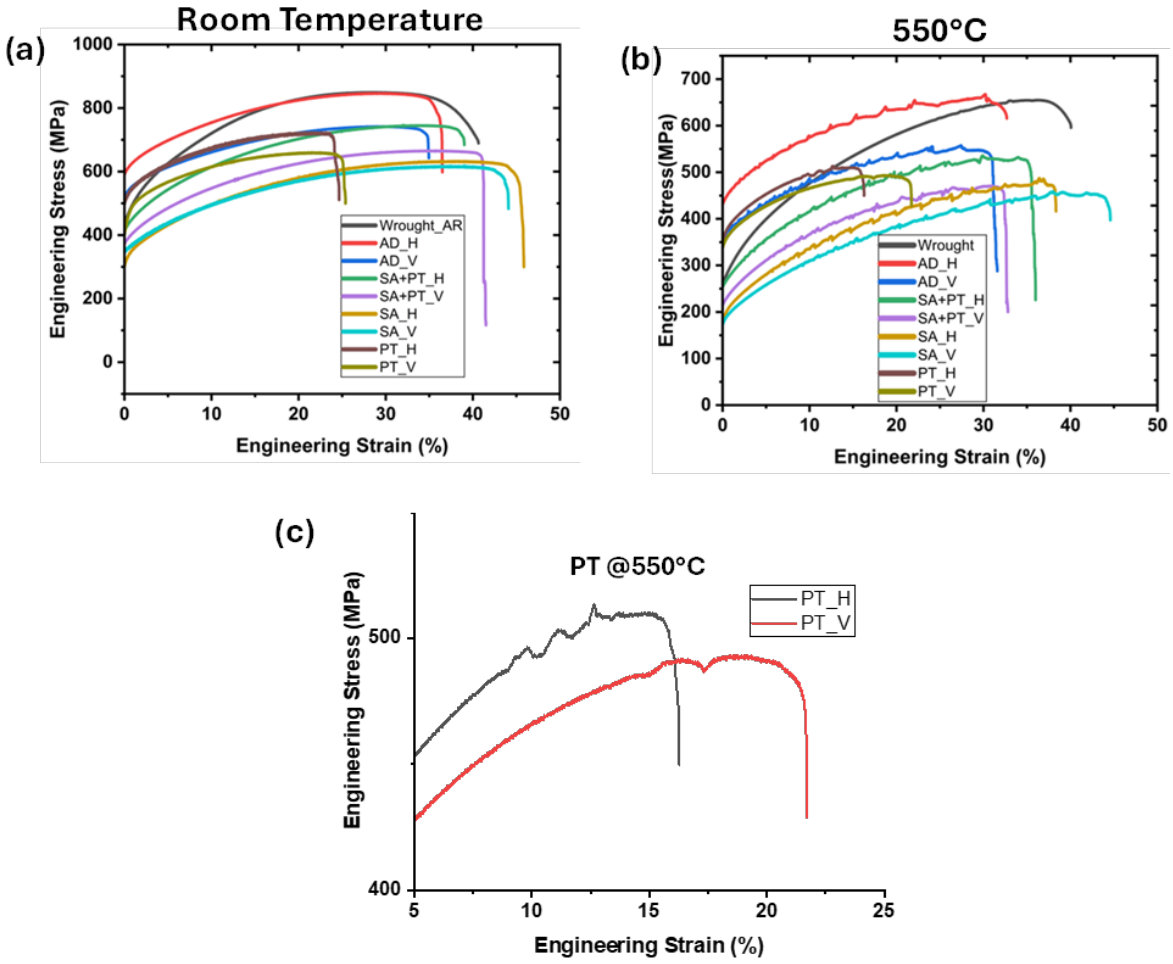


Figure 2. Representative Engineering Stress–Strain Curves for DED-Fabricated Alloy 709, Benchmarked Against Wrought Materials. The results illustrate the effects of post-build heat treatment and horizontal (H) and vertical (V) specimen orientations on tensile strength, strain hardening, and ductility.

The AD material exhibited the highest strength among the LP-DED conditions. AD-H reached an ultimate tensile strength (UTS) of approximately 850 MPa at RT and 650 MPa at 550°C, approaching or exceeding the wrought benchmark, while AD-V showed consistently lower flow stress and ultimate strength. Both orientations nevertheless retained fracture strains above 30%, with stress rising over a broad strain range prior to necking, indicating substantial strain-hardening capacity.

Post-build heat treatment produced a trade-off between strength and ductility. Specimens that were solution-annealed showed the lowest flow stress and ultimate strength but the largest fracture strains, reaching approximately 40–45% engineering strain in both orientations. The combined SA+PT treatment gave an intermediate response, with strength above SA but below AD-H and ductility of approximately 30–40%, representing the most balanced strength–elongation combination among the heat-treated conditions. Precipitation-treated specimens showed the most limited elongation, failing at approximately 18–25% strain; although PT raised the flow stress relative to SA, it did not restore the UTS of AD-H.

Horizontal specimens generally exhibited higher flow stress, higher UTS, and stronger strain hardening than vertical specimens, consistent with the layer-wise deposition architecture, in which vertical loading places build-layer interfaces and elongated solidification features unfavorably relative to the tensile axis. This anisotropy was most pronounced in the AD condition and was reduced, although not eliminated, by solution annealing.

Relative to wrought Alloy 709, AD-H matched or exceeded the wrought strength, while solution-annealed material exceeded it in fracture strain but at lower strength; the wrought material retained the most balanced combination of strain hardening, strength and ductility. The results therefore show that LP-DED Alloy 709 can achieve wrought-comparable tensile behavior, but that the response depends strongly on both build orientation and post-build heat treatment.

Figure 3 compares the retention of tensile properties at 550°C relative to RT for LP-DED Alloy 709, expressed as the yield-strength retention ratio (YS-550°C/YS-RT) and the elongation retention ratio (EL-550°C/EL-RT).

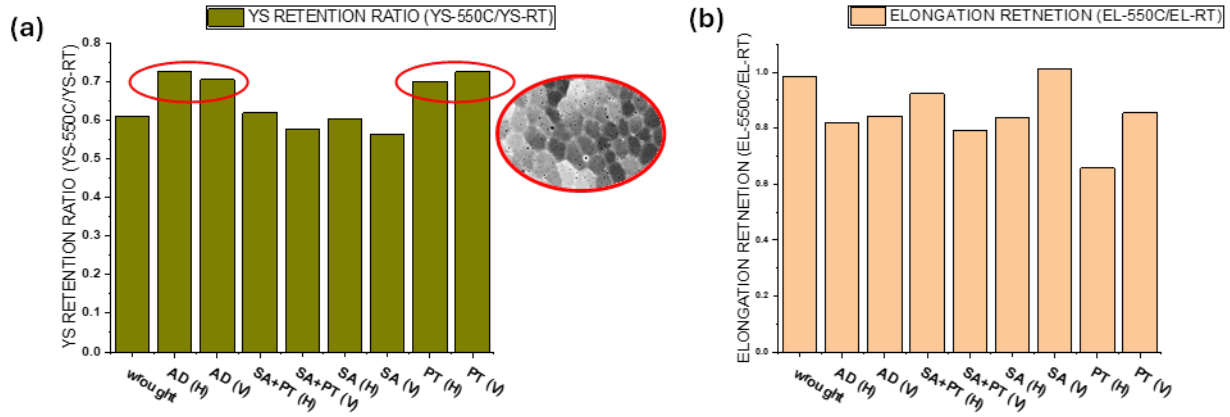


Figure 3. Comparison of the Measured Responses of DED-Fabricated A709 Steel Under Different Processing Conditions. Red ellipses identify the selected conditions, while the inset shows a representative SEM micrograph of the corresponding microstructure.

The AD and PT conditions, highlighted by the red ellipses, retained yield strength most effectively, with ratios of approximately 0.70–0.73 compared with 0.61 for wrought Alloy 709 and 0.56–0.62 for SA and SA+PT. These are the two conditions in which the deposition-induced cellular substructure is retained: AD preserves it intact, while PT ages the material at 775°C without a preceding solution anneal. By contrast, SA and SA+PT, in which the cellular network has been dissolved at 1150°C, showed the lowest retention of any LP-DED condition. This correlation indicates that the fine network of solute-enriched cell boundaries and retained

dislocations provides obstacles to dislocation motion that remain effective at 550°C and resist thermal softening more successfully than a recrystallized matrix strengthened by precipitation alone. The inset micrograph confirms the presence of this cellular architecture, with distinct cell boundaries and dispersed second-phase features.

Elongation retention followed a different ranking, with SA highest (~1.01) and PT-H lowest (~0.86); AD and PT retained ~0.82–0.85 against ~0.98 for wrought material. The conditions best able to retain strength were therefore not those best able to retain ductility. These results indicate that complete homogenization of the deposition substructure is not automatically optimal for elevated-temperature strength. However, given the accompanying loss of ductility retention and the metastability of the cellular substructure under prolonged exposure, this advantage cannot be assumed to persist in service and must be assessed by creep testing.

Figure 4 shows low- and high-magnification SEM fractographs of the tensile fracture surfaces obtained from the different processing conditions. All specimens displayed rough, irregular fracture surfaces with no evidence of flat cleavage facets, indicating that fracture proceeded by a ductile mechanism rather than brittle separation. At higher magnification, the surfaces were covered by well-developed dimples formed through micro-void nucleation, growth, and eventual coalescence. Differences in dimple size, depth, and uniformity between conditions reflect local variations in microstructure and plastic deformation capacity, with finer and more uniform dimples generally corresponding to greater tensile ductility.

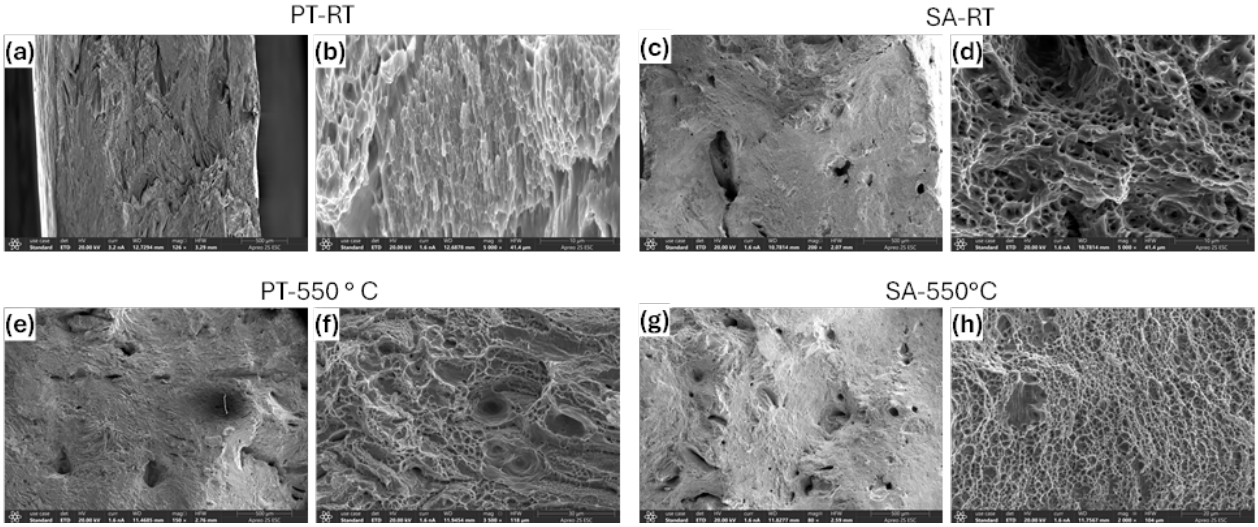


Figure 4. Fractographs Showing Low- and High-Magnification Views of the Tensile Fracture Surfaces. The images reveal a predominantly ductile fracture characterized by micro-void nucleation, growth, and coalescence, along with localized pores and processing-related defects.

3.2 Creep Response of LP-DED Alloy 709

Figure 5 presents creep elongation–time curves for LP-DED A709 tested between 650 and 750°C at applied stresses of 140–311 MPa, together with representative typical transmission electron microscopy (TEM) observations of the SA and SA+PT microstructure. The corresponding rupture lives, elongations, and reduction-in-area values are summarized in Table 3.

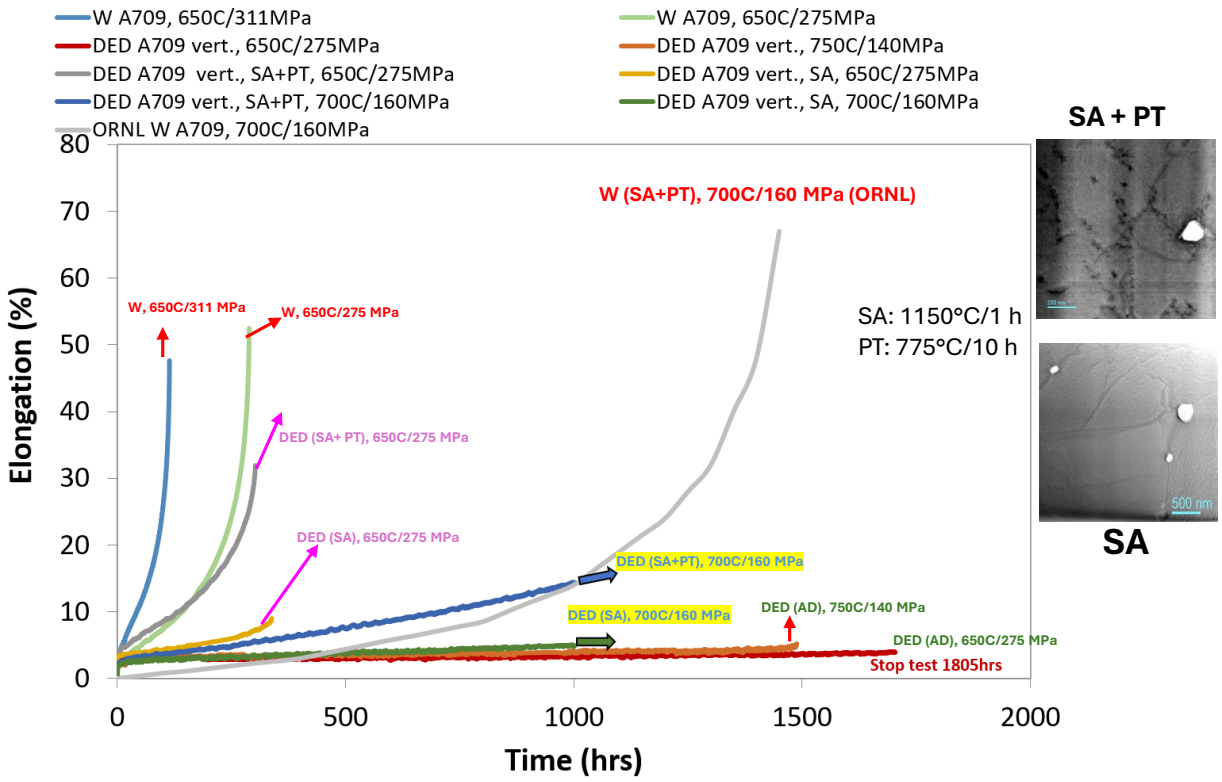


Figure 5. Creep Properties and Post-Creep Fractography of DED-Fabricated A709 Steel Under Different Heat-Treatment, Temperature, and Applied-Stress Conditions. The creep elongation–time curves compare DED and wrought A709 tested at 650-750°C and 140–311 MPa, illustrating the effects of processing condition and heat treatment on creep deformation, rupture life, and fracture behavior.

Wrought reference behavior. The wrought material exhibited a short primary stage, a well-defined secondary regime and a pronounced tertiary acceleration terminating in rupture. At 650°C/311 MPa, rupture occurred after 115 h with 48% elongation and 50.7% RA. At 650°C/275 MPa, rupture occurred after 290 h with 55% elongation and 56.6% RA. The wrought SA+PT reference tested at 700°C/160 MPa ruptured after 1450 h with 67% elongation following an extended secondary stage and a sharp tertiary acceleration.

As-deposited condition. The AD-V specimen tested at 650°C/275 MPa accumulated 2.3% diameter reduction and 4.5% RA over 1805 h, at which point the test was terminated; the creep curve remained flat throughout, with no tertiary acceleration observed. The AD-V specimen tested at 750°C/140 MPa remained intact beyond 1500 h with comparably low strain accumulation. No rupture elongation values were obtained for either AD specimen.

Heat-treated conditions. At 650°C/275 MPa, the SA specimen ruptured after 180 h with 9% elongation, 4.4% diameter reduction, and 8.6% RA. Under the same conditions, the SA+PT specimen ruptured after 350 h with 33% elongation, 16.5% diameter reduction, and 30.3% RA. At 700°C/160 MPa, the SA and SA+PT specimens had accumulated approximately 4–8% strain after 340 and 425 h, respectively; these tests were in progress at the time of reporting.

Table 3. Summary of Creep-Test Conditions and Results for Wrought and Vertically Built DED A709 Steel in the As-Deposited (AD), Stress-Annealed (SA), and Stress-Annealed Plus Post-Treated (SA+PT) Conditions. An asterisk indicates an ongoing test duration at the time of reporting.

Sample #	Sample ID	Build Orientation	Heat Treatment	Test Condition	Time (h)	El (%)	Diameter Reduction (%)	Reduction in Area (%)	Status	Notes
1	Wrought			650°C/311 MPa	115	48	29.78	50.696	Tested	
3	Wrought			750°C/140 MPa	303	52			Tested	
7	AD-V-02	Vertical	AD	750°C/140 MPa	1500*	~			Ongoing	
2	Wrought			650°C/275 MPa	290	55	34.11	56.587	Tested	
4	AD-V-01	Vertical	AD	650°C/275 MPa	1805	~	2.267	4.4820	Stopped	XCT afterward
5	SA-V-02	Vertical	SA	650°C/275 MPa	180	**9**	4.400	8.6064	Tested	
6	SA+PT-V-02	Vertical	SA+PT	650°C/275 MPa	350	**3**3	16.50	30.278	Tested	
7	Wrought ORNL		SA+PT	700°C/160 MPa	1450	**67**				
8	SA-V-03	Vertical	SA	700°C/160 MPa	340				Ongoing	XCT first
9	SA+PT-V-03	Vertical	SA+PT	700°C/160 MPa	425				Ongoing	XCT first

Comparison of measured values. Table 3 shows that, under the matched condition of 650°C/275 MPa, rupture life increased in the order SA (180 h) < wrought (290 h) < SA+PT (350 h), while elongation increased in the order SA (9%) < SA+PT (33%) < wrought (55%) and RA followed the same ranking (8.6%, 30.3%, 56.6%). The AD specimen exceeded all ruptured conditions in test duration but yielded no elongation value.

Taken together, the results indicate the following:

- AD A709 accumulated very little creep strain, remaining intact beyond 1500–1805 h at 650°C/275 MPa and 750°C/140 MPa; however, these tests did not reach rupture, so no creep elongation was obtained and the ability of this condition to accommodate creep strain remains unestablished.
- SA+PT accommodated creep strain substantially better than either SA or AD, reaching 33% elongation and 30.3% RA at rupture, compared with 9% and 8.6% for SA and no measurable elongation for AD.
- SA+PT also doubled the rupture life of SA (350 h versus 180 h) and exceeded the wrought reference (290 h) under the same conditions, so the improvement in creep strain accommodation was obtained without any penalty in rupture life.
- Wrought A709 failed with the highest elongation and RA (55% and 56.6%), while the SA condition failed at considerably lower creep strains, indicating greater susceptibility to localized boundary damage; SA+PT lies between these two extremes and is the closest of the LP-DED conditions to wrought-like ductile creep behavior.

Figure 6 shows photographs of ruptured creep specimens of wrought and LP-DED A709 tested under different temperature-stress conditions. The macroscopic fracture morphology provides direct visual confirmation of the ductility trends quantified by the elongation and reduction-in-area measurements.

The wrought specimens exhibited pronounced macroscopic ductility. At 650°C/311 MPa (116.5 h), the gauge section developed a sharp, localized neck terminating in a chisel-edge rupture, indicating plasticity-controlled failure by necking instability. At 650°C/275 MPa (290.6 h), extensive uniform elongation accompanied the neck, consistent with the measured elongation (55%) and RA (57%). The long-duration test at 725°C/100 MPa (2103 h) showed more uniform gauge-section deformation with a diffuse neck, reflecting the transition toward lower-stress, diffusion-assisted creep. The fracture occurred within the reduced gauge section, confirming that failure was governed by bulk creep deformation rather than by local stress concentrators.

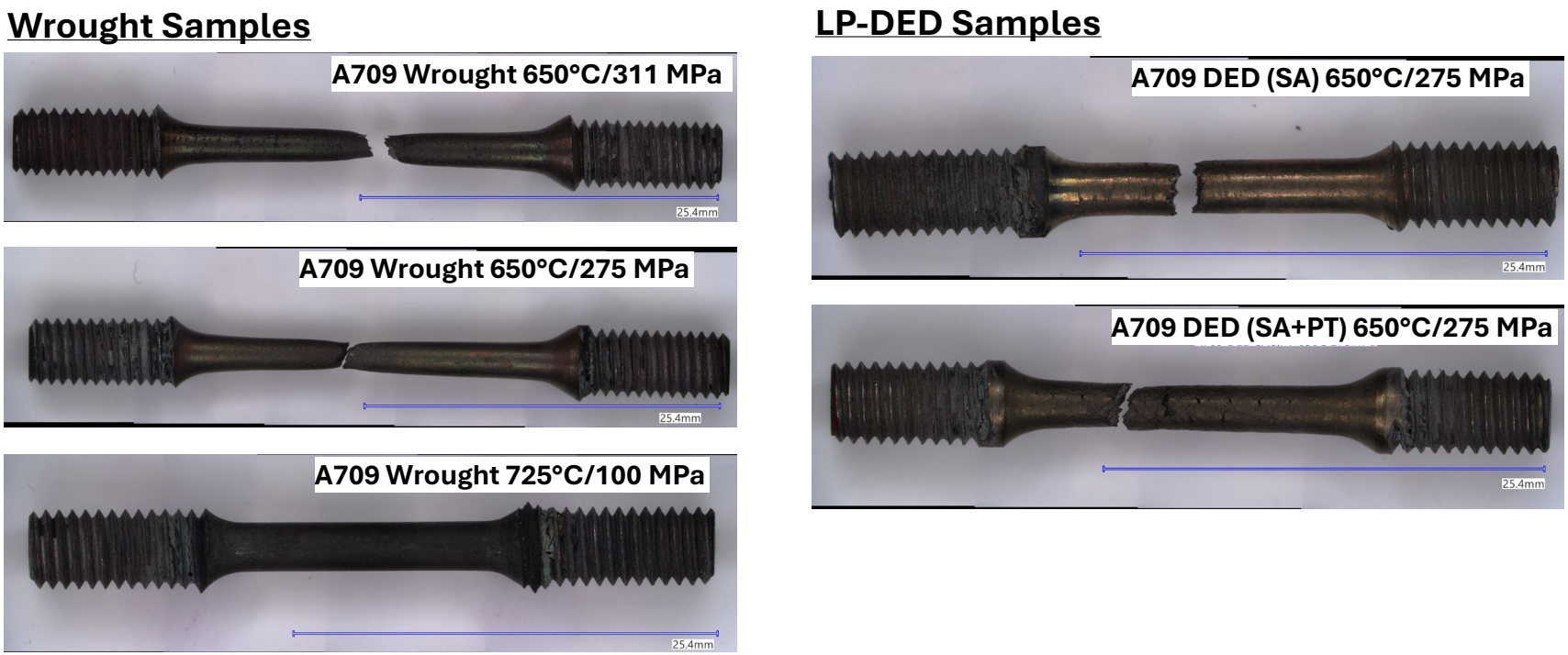


Figure 6 Photographs of Failed Creep Specimens of Wrought and DED-Fabricated A709 Steel After Testing Under Various Temperature–Stress Conditions. The specimens show differences in creep deformation, necking, and fracture location as a function of material condition and heat treatment, including stress annealing (SA) and stress annealing plus post-treatment (SA+PT). Scale bar: 25.4 mm.

The LP-DED specimens behaved differently. The SA specimen tested at 650°C/275 MPa failed after only 180 h with minimal necking and a comparatively flat fracture normal to the loading axis. The flat, low-contraction morphology is consistent with the low ductility (9% elongation, 8.6% RA); the underlying fracture mechanism requires further investigation. The SA+PT specimen showed markedly greater localized contraction and a more deformed fracture region, consistent with its higher elongation (33%) and RA (30%), indicating that precipitation strengthening restored sufficient intragranular resistance to dislocation motion to distribute deformation more uniformly and delay cavity coalescence, although necking remained less extensive than in the wrought material.

Figure 7 presents XCT reconstructions of the gauge sections of wrought and LP-DED A709 specimens prior to creep testing, providing a non-destructive baseline of the internal defect population. The wrought material (Figure 7a, d) appears essentially fully dense in both the transverse and longitudinal views, with no resolvable porosity above the detection limit of the scan, consistent with the homogeneous microstructure expected from thermomechanical processing. In contrast, both LP-DED conditions contain discrete internal voids distributed throughout the gauge volume. The transverse slices (Figure 7b, c) reveal a small number of irregularly shaped pores of a few tens of micrometres in size, several of which are located near the specimen surface where subsurface defects are most detrimental to load-bearing capability. The longitudinal reconstructions (Figure 7e, f) show that these defects are dispersed along the build direction rather than concentrated at a single interface, with some appearing slightly elongated and irregular in morphology, indicative of lack-of-fusion between adjacent deposition tracks or layers rather than spherical gas porosity. Comparison of the SA (Figure 7b, e) and SA+PT (Figure 7c, f) conditions shows a broadly similar defect population, confirming that post-build heat treatment modifies the matrix microstructure and precipitate state but does not eliminate or significantly heal process-induced porosity. The persistence of these defects is mechanically significant, as pores act as stress concentrators and preferential cavity-nucleation sites during high-temperature deformation, and their non-uniform axial distribution provides a plausible explanation for the off-center creep fractures observed in the DED specimens. Post-mortem XCT of ruptured and interrupted specimens is therefore required to determine whether creep damage initiates preferentially at these pre-existing defects or nucleates independently at grain and prior-layer boundaries.

Figure 8 compares the creep fracture surfaces of wrought and LP-DED A709 tested under identical conditions of 650°C/275 MPa, allowing the influence of processing route and heat treatment on the damage mechanism to be isolated. The wrought specimen (Figure 8a) exhibits a heavily cavitated fracture surface at low magnification, with a pronounced peripheral shear lip and evidence of substantial macroscopic contraction consistent with its high measured RA (57%). At high magnification, the surface shows rounded cavities of varying sizes within a fine dimpled matrix. These features suggest cavity growth and coalescence alongside plastic deformation, although the detailed fracture mechanism requires further investigation. This morphology is characteristic of ductile, deformation-controlled creep rupture and correlates well with the long tertiary stage observed in the corresponding creep curve.

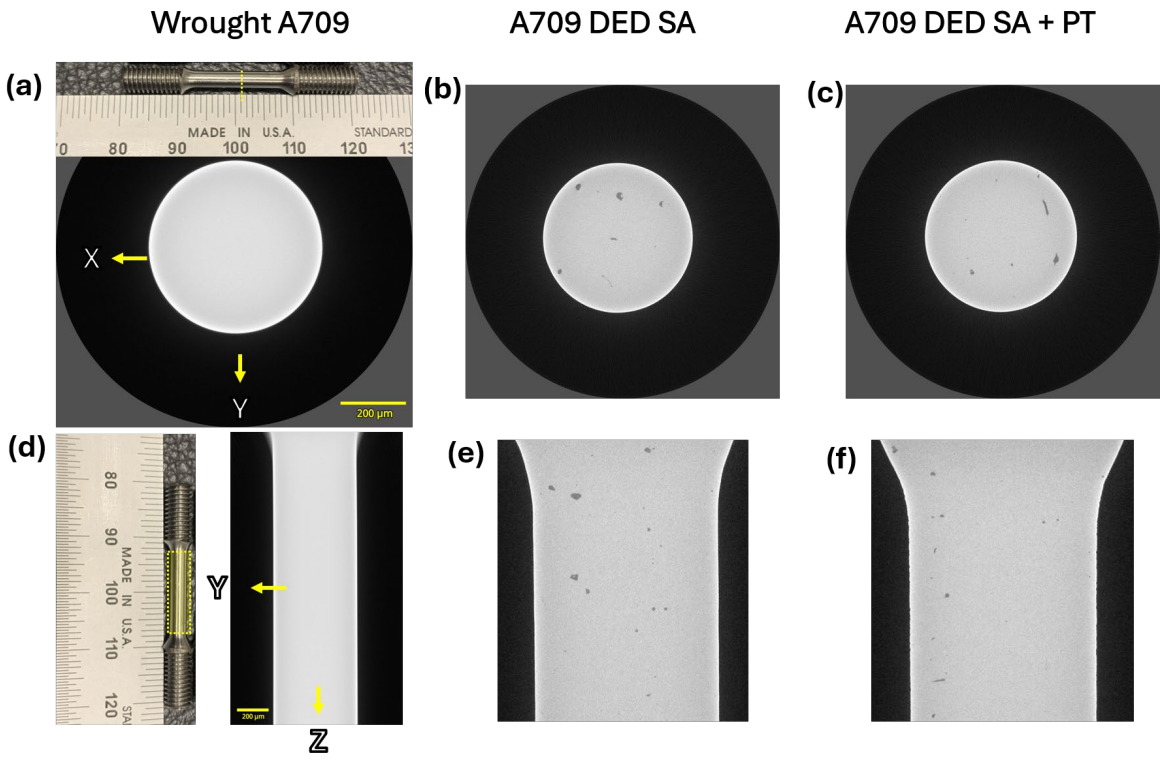


Figure 7 X-Ray Computed Tomography (XCT) Reconstructions of the Gauge Sections of Pre-Creep Tensile/Creep Specimens. (a, d) Wrought A709, (b, e) LP-DED A709 in the solution-annealed (SA) condition, and (c, f) LP-DED A709 in the solution-annealed plus precipitation-treated (SA+PT) condition. Top row (a–c) shows representative transverse (X–Y) cross-sectional slices; bottom row (d–f) shows longitudinal (Y–Z) slices along the loading/build direction. Insets in (a) and (d) indicate the interrogated gauge region relative to the specimen geometry. Dark contrast features correspond to internal porosity and lack-of-fusion defects.

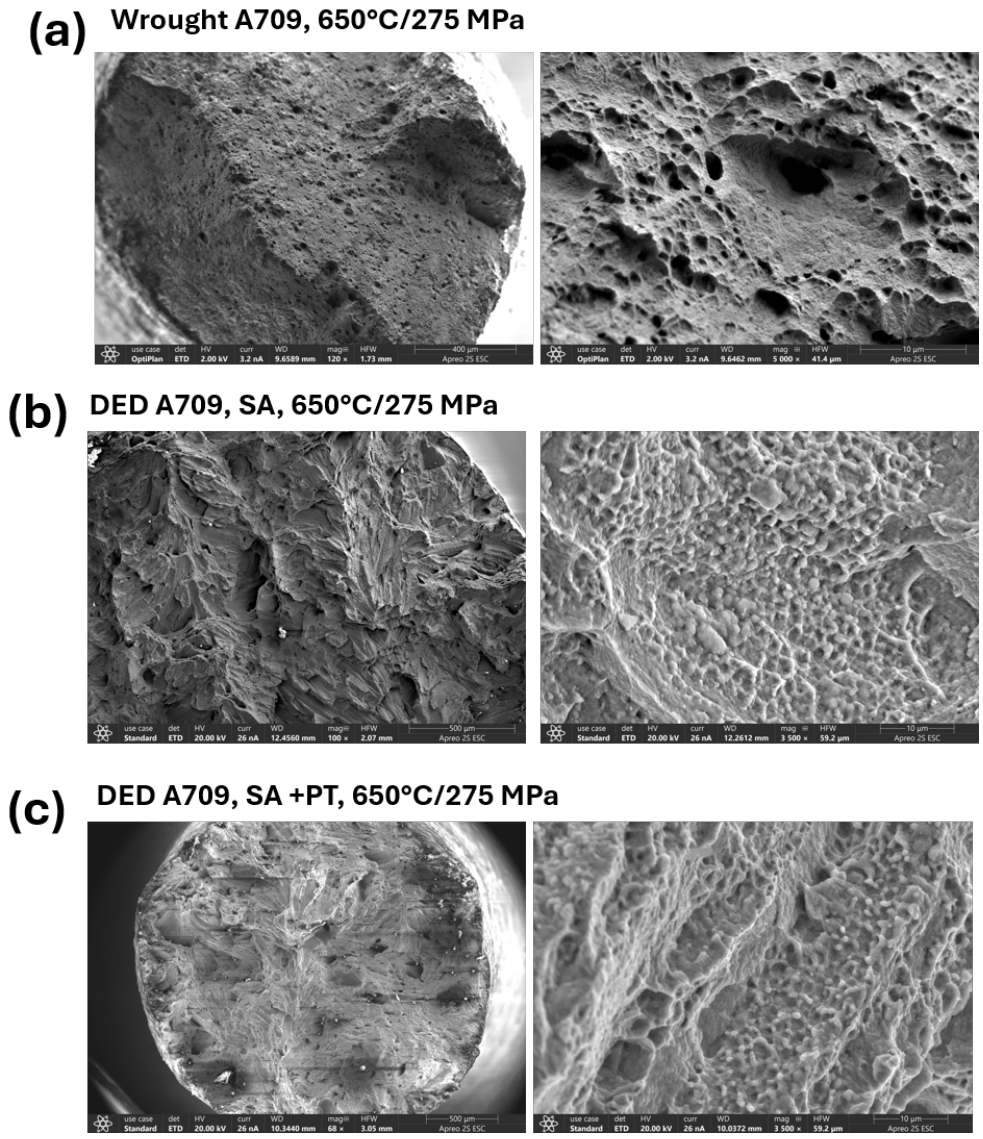


Figure 8. SEM fractographs of Creep-Ruptured A709 Specimens Tested at 650°C/275 MPa, Shown at Low Magnification (left) and High Magnification (right). (a) Wrought A709, (b) LP-DED A709 in the solution-annealed (SA) condition, and (c) LP-DED A709 in the solution-annealed plus precipitation-treated (SA+PT) condition.

In contrast, the DED SA specimen (Figure 8b) displays a markedly different low-magnification morphology, consisting of a comparatively flat fracture plane with faceted, blocky regions and coarse ridges that appear to follow prior grain and interlayer boundaries. At higher magnification, regions of fine dimpling are interspersed with smoother, boundary-associated facets, indicating a mixed-mode fracture in which intergranular decohesion contributed significantly alongside localized micro-void coalescence. The absence of a strengthening intragranular substructure in the solution-annealed state concentrates deformation at boundaries, so that cavities nucleate and link along these interfaces before appreciable bulk plasticity can accumulate, producing the short rupture life and low-ductility failure recorded for this condition.

The DED SA+PT specimen (Figure 8c) exhibits an intermediate character. The low-magnification image shows a more uniformly rough fracture surface with a well-developed peripheral shear lip and radial features converging toward the interior, indicating that a greater degree of plastic deformation preceded final separation, consistent with its improved elongation (33%) and RA (30%). At high magnification, rounded cavities of varying sizes appear within a fine dimpled matrix, suggesting that cavity growth and coalescence occurred alongside plastic deformation. Atom Probe Tomography of Precipitation-Treated Alloy 709

Figure 9 presents the APT reconstruction of LP-DED A709 in the PT condition (before any tensile or creep exposure), so that the observed solute distribution reflects the microstructure produced by the heat treatment itself rather than any deformation- or service-induced evolution.

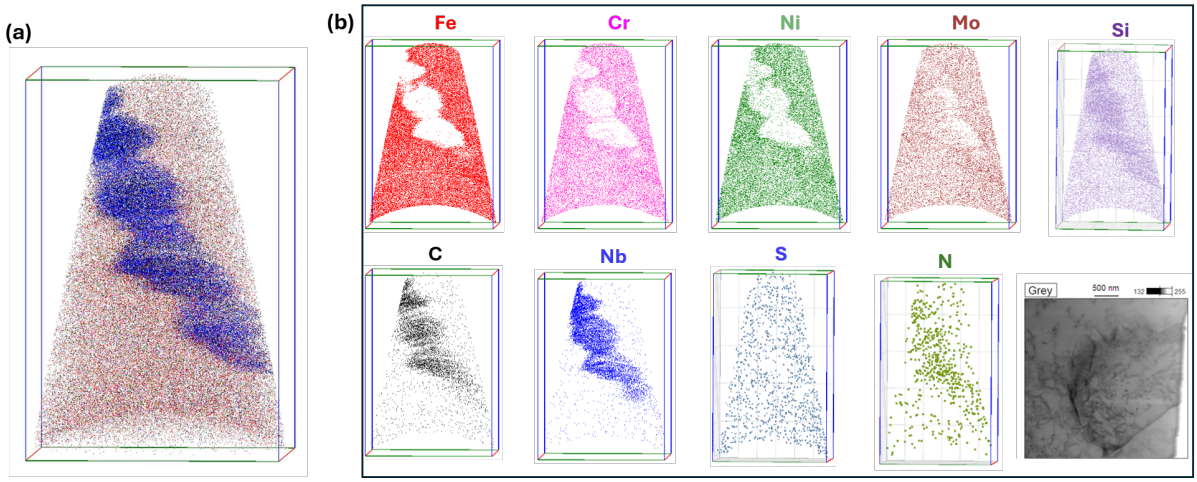


Figure 9. Atom Probe Tomography (APT) Analysis of LP-DED A709 in the As-Heat-Treated Precipitation-Treated (PT) Condition, Prior to Mechanical Testing. (a) Three-dimensional reconstruction of the APT tip showing the spatial distribution of the matrix and a solute-enriched feature (Nb atoms in blue). (b) Individual elemental atom maps for Fe, Cr, Ni, Mo, Si, C, Nb, S and N extracted from the same reconstruction, together with a TEM image of the corresponding needle geometry.

The three-dimensional reconstruction in Figure 9(a) reveals a well-defined, irregularly shaped solute-enriched region extending diagonally through the analyzed volume, embedded within an otherwise uniform austenitic matrix. The corresponding elemental maps in Figure 9(b) show that this feature is strongly enriched in Nb and C, which are co-located within the same volume, while Fe, Cr, Ni and Mo are simultaneously depleted in exactly the same region, appearing as clear voids in their respective atom maps.

Si is distributed relatively uniformly throughout the volume with only weak association with the precipitate, while the low-abundance species S and N are present as sparse, dilute distributions; N shows a slight tendency toward the precipitate region consistent with Cr-rich carbide or Cr-enriched boundary segregation was detected within the analyzed volume, although the limited field of view of APT means that such phases cannot be excluded elsewhere in the microstructure.

Such particles are highly thermodynamically stable and coarsen slowly at elevated temperature and are therefore expected to provide effective obstacles to intragranular dislocation glide and climb during creep. This finding provides a direct microstructural explanation for the superior creep rupture life and creep ductility of the SA+PT condition relative to the SA condition, in which the absence of a comparable intragranular precipitate dispersion forces strain to localize at grain and prior-layer boundaries.

Figure 10 quantifies the local chemistry of the precipitate and surrounding matrix in as-heat-treated PT condition.

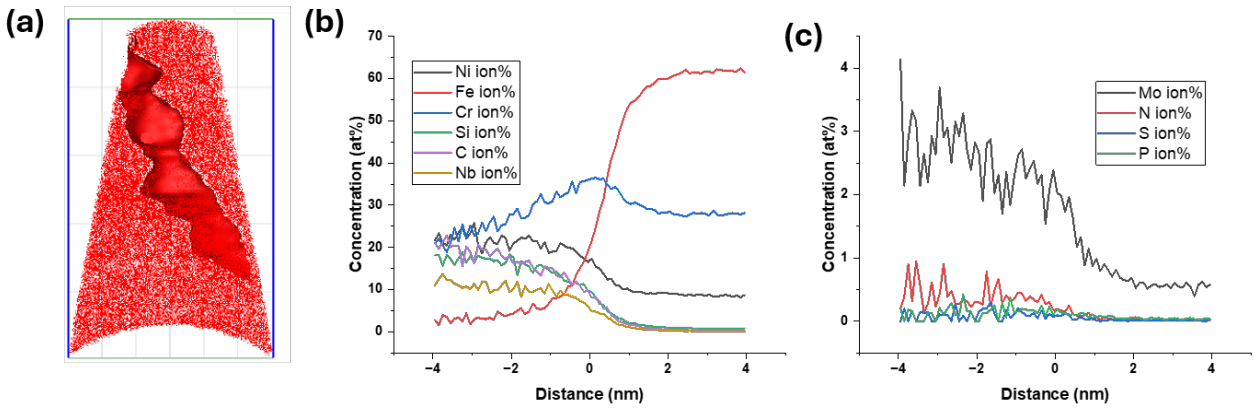


Figure 10. Quantitative Atom Probe Tomography (APT) Analysis of LP-DED A709 in the As-Heat-Treated Precipitation-Treated (PT) condition, Prior to Mechanical Testing. (a) Iso-concentration surface delineating the precipitate/matrix interface within the reconstructed volume (Fe atoms shown in red). (b, c) Proximity histograms (proxigrams) computed normal to the iso-surface showing the concentration profiles of (b) the major alloying and interstitial species (Ni, Fe, Cr, Si, C, Nb) and (c) the minor species (Mo, N, S, P).

The proxigrams reveal a chemically abrupt interface with a transition width of only ~1–2 nm, indicating a discrete, well-defined particle rather than a diffuse solute cluster. Among the minor species, N reaches ~0.8 at.% and shows a modest association with the precipitate, while S and P remain at trace levels throughout.

The pronounced co-enrichment of Nb and C, accompanied by depletion of the matrix-forming elements, confirms that the precipitation treatment produces stable Nb- and C-rich particles within the austenite matrix. Notably, no Cr depletion is observed in the matrix adjacent to the interface, indicating that precipitation does not locally impoverish the matrix in Cr and therefore should not compromise oxidation or corrosion resistance. Such Nb- and C-rich particles are expected to be highly coarsening-resistant at 650–750°C and to act as effective obstacles to dislocation glide and climb, providing a direct microstructural explanation for the improved creep rupture life and creep ductility of the SA+PT condition relative to SA-only material. Correlative TEM and additional APT datasets are required to obtain statistically meaningful precipitate size distributions, number densities and interparticle spacings for input into quantitative strengthening models.

3.3 Tensile Response of LP-DED Grade 92

Testing carried out in FY 2026 completed the N and N+T conditions, thereby completing the tensile test matrix for LP-DED G-92 across all heat-treatment conditions and both build orientations.

As a martensitic 9Cr steel, the AD strength of G-92 is dominated by untempered martensite formed during the rapid cooling and cyclic reheating inherent to DED. Accordingly, the AD condition was by far the strongest, with AD-H and AD-V reaching approximately 1650 and 1580 MPa at RT but fracturing at only 10–16% strain (Figure 11a) after a short hardening stage, behavior typical of a high-dislocation-density, carbon-supersaturated matrix. Tempering alone reduced strength to approximately 900–1000 MPa through recovery of the martensitic substructure and carbide precipitation. The N condition retained relatively high strength (N-H ≈ 1,300 MPa) with continuous hardening to 12–13% strain, consistent with fresh martensite formed on cooling from the austenitizing temperature, while N+T gave the lowest strength (approximately 600–650 MPa) but the greatest elongation (14–18%), representing the fully tempered microstructure intended for service.

Horizontal specimens were consistently stronger than vertical ones. This anisotropy was largest in the AD and N conditions and smallest after N+T, indicating that austenitization and tempering partially homogenize the deposited microstructure.

At elevated temperature (Figure 11b), all conditions showed reduced flow stress and contracted hardening. The AD specimens remained strongest (approximately 1,250–1,350 MPa) but failed at only 4–5% strain, indicating pronounced loss of ductility. N-H provided the best combination, sustaining approximately 1,250 MPa to nearly 15% elongation, whereas the tempered and N+T conditions reached only 400–700 MPa with 8–11% elongation and exhibited early peak stresses followed by extended decline. Overall, the completed tensile tests for all heat treated conditions reveal a clear heat-treatment-controlled strength–ductility trade-off: AD offers exceptional strength but inadequate ductility and thermal stability, N+T provides the ductility and stability required for service at the expense of strength, and the N condition offers the most attractive intermediate balance, particularly in the horizontal orientation at elevated temperature.

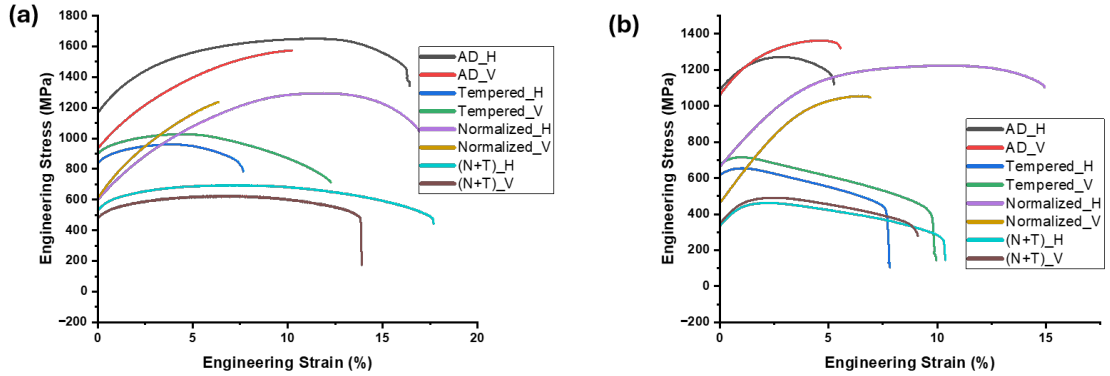


Figure 11. Representative Engineering Stress–Strain Curves for LP-DED-Fabricated Grade 92 (G-92) Steel Tested at (a) Room Temperature and (b) Elevated Temperature. The figures compare the as-deposited (AD), tempered, normalized (N), and normalized-plus-tempered (N+T) conditions for horizontal (H) and vertical (V) build orientations.

Figure 12 quantifies how effectively each condition retains its room-temperature tensile properties at 550°C. The N condition showed the highest yield-strength retention (approximately 0.95–0.98 for N-H and N-V), closely followed by the AD material (approximately 0.91–0.94), indicating that the martensitic matrix in both conditions resists thermal softening effectively. The tempered condition retained approximately 0.73–0.75, while N+T showed the lowest retention, with N+T-H falling to approximately 0.61. This trend reflects the fact that fully tempered microstructures have already undergone substantial recovery and carbide coarsening, leaving less capacity to sustain strength at elevated temperature.

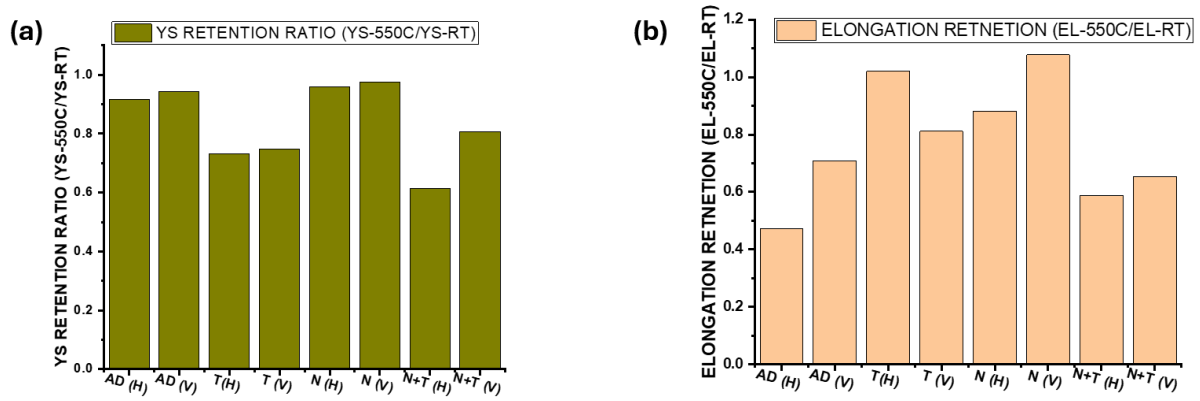


Figure 12. Retention of Tensile Properties at 550°C Relative to Room Temperature for LP-DED Grade 92 Steel. (a) Yield strength retention ratio (YS-550°C/YS-RT) and (b) elongation retention ratio (EL-550°C/EL-RT)

Elongation retention followed a different ranking. The N-V and T-H conditions retained or slightly exceeded their room-temperature ductility (ratios of approximately 1.03–1.08), indicating enhanced plasticity at 550°C through thermally assisted deformation. In contrast, AD-H exhibited the lowest retention (approximately 0.47), consistent with the very limited elongation observed for AD specimens at temperature. The N+T conditions retained only approximately 0.59–0.66, showing that superior room-temperature ductility does not necessarily translate into ductility retention at temperature.

Build orientation influenced both metrics, with vertical specimens generally exhibiting equal or better retention than horizontal ones despite their lower absolute strength. Taken together, the N condition provides the most balanced retention behavior, combining near-complete strength retention with preserved ductility, and therefore represents the most promising candidate for elevated-temperature application among the conditions evaluated.

Figure 13 compares the tensile fracture surfaces of the N and N+NT conditions at both test temperatures. At RT, the N+T specimen (Figure 13a, b) exhibits a rough, irregular surface covered by well-developed dimples together with several large, near-spherical pores of tens to hundreds of micrometres in diameter. The dimpled morphology confirms failure by micro-void nucleation, growth and coalescence within a fully tempered martensitic matrix, consistent with the high elongation measured for this condition. The N specimen at RT (Figure 13c,d) shows a comparatively coarser and more heterogeneous surface, with regions of shallow dimpling interspersed with smoother, flatter facets. This mixed morphology reflects the lower ductility and higher strength of the untempered martensitic matrix.

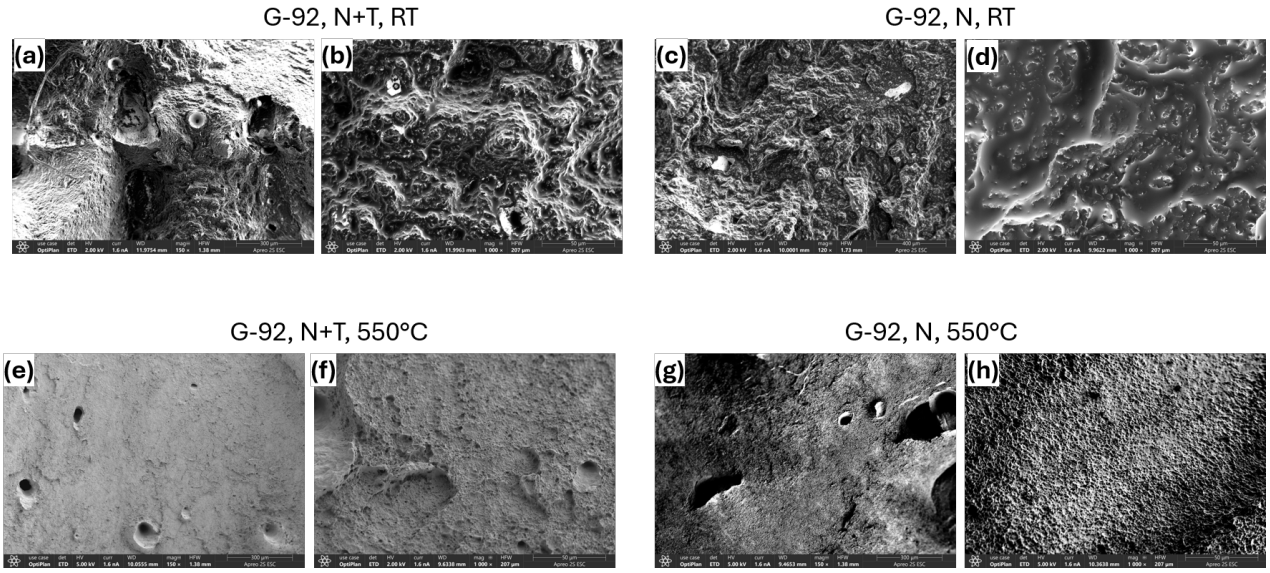


Figure 13. SEM Fractographs of Tensile-Tested LP-DED Grade 92 Steel at Low And High Magnification. (a, b) Normalized-plus-tempered (N+T) tested at room temperature, (c, d) normalized (N) tested at room temperature, (e, f) N+T tested at 550°C, and (g, h) N tested at 550°C.

At 550°C, both conditions retain a fundamentally ductile character but with notable differences in scale. The N+T specimen (Figure 13e, f) displays a relatively flat, smooth surface with sparse, shallow dimples and isolated voids, indicating that deformation became more localized and that void growth was less extensive prior to separation, consistent with the reduced elongation retention measured for this condition. In contrast, the N specimen at 550°C (Figure 13g, h) exhibits a uniformly fine, densely dimpled surface at high magnification, indicating extensive and homogeneously distributed micro-void coalescence, in agreement with its superior elongation retention at temperature.

3.4 Creep Benchmarking of LP-DED Grade 91 and Grade 92

Figure 14 shows the machined creep specimens prepared from LP-DED G-92 and G-91 steel deposits. Both sets were extracted from the as-built blocks and machined to a uniform threaded-end, reduced-gauge geometry to ensure consistent load transfer and confine deformation to the gauge section. The specimens are free of visible machining damage or surface defects and show good dimensional uniformity, which is essential for minimizing scatter in rupture-life measurements. Specimens have been prepared for vertical orientations and the selected post-build heat-treatment conditions.

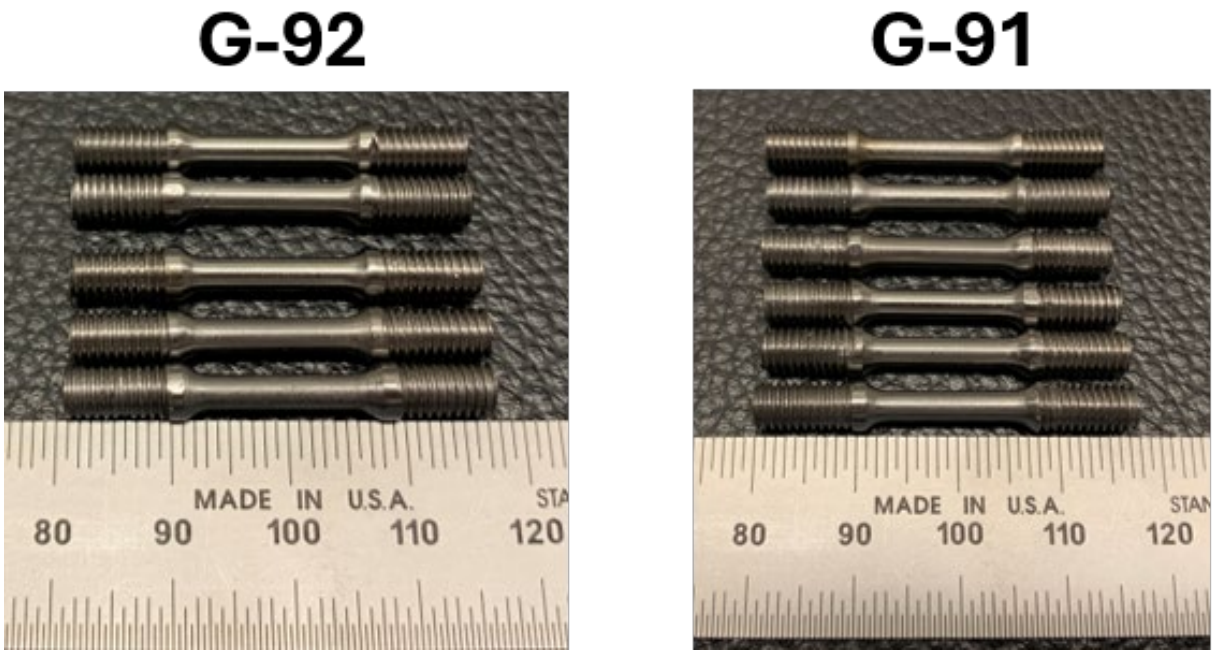


Figure 14. Photographs of Machined, Threaded-End Creep Specimens Prepared from LP-DED-Fabricated Grade 92 (G-92, left) and Grade 91 (G-91, right) Steels

Creep testing is planned as the next stage of the program and will extend the characterization of these 9Cr martensitic steels from short-term tensile behavior to long-term, time-dependent deformation. Tests will be performed at service-relevant temperatures and stresses to establish minimum creep rates, rupture lives, and creep ductility for each condition. Because the tensile results indicate that the N and N+NT conditions differ markedly in microstructural stability, the creep data are expected to be decisive in selecting the appropriate post-build heat treatment.

Two temperature–stress combinations, 650°C/140 MPa and 600°C/220 MPa, are selected for all heat-treatment conditions. These creep parameters cover the intended service envelope of 9Cr martensitic steels while producing rupture within a practically accessible timeframe.

The wrought rupture lives of 743 h at 650°C/140 MPa [13] and 475 h at 600°C/220 MPa [14] were taken from published data for conventionally processed material in the standard normalized-and-tempered condition, which represents the qualified service microstructure and therefore the appropriate baseline. References were selected such that the reported compositions and heat-treatment schedules conform to specification and, critically, that the test conditions match the present matrix exactly, avoiding any need for extrapolation. This enables a direct assessment of whether LP-DED material meets or exceeds wrought creep performance under identical loading. Creep ductility will be recorded alongside rupture life, as it is expected to be equally discriminating in distinguishing additively manufactured material from its wrought counterpart (see Table 4).

Table 4. Planned Creep Test Matrix for LP-DED-Fabricated Grade 91 and Grade 92 Steels. The table shows selected temperature–stress combinations for the as-deposited (AD), normalized (N), and normalized-plus-tempered (N+T) conditions.

Condition	Temperature/Stress	Rupture Time (h)
As-Deposited	650°C/140 MPa	Wrought: 743 [13]
As-Deposited	600°C/220 MPa	Wrought: 475 [14]
Normalized (N)	650°C/140 MPa	
Normalized (N)	600°C/220 MPa	
N+ Tempering	650°C/140 MPa	
N+ Tempering	600°C/220 MPa	

3.5 Atom Probe Tomography of Normalized-and-Tempered Grade 92

Figure 15 presents the APT reconstruction of LP-DED Grade 92 in the N+T condition, which represents the intended service microstructure for this alloy.

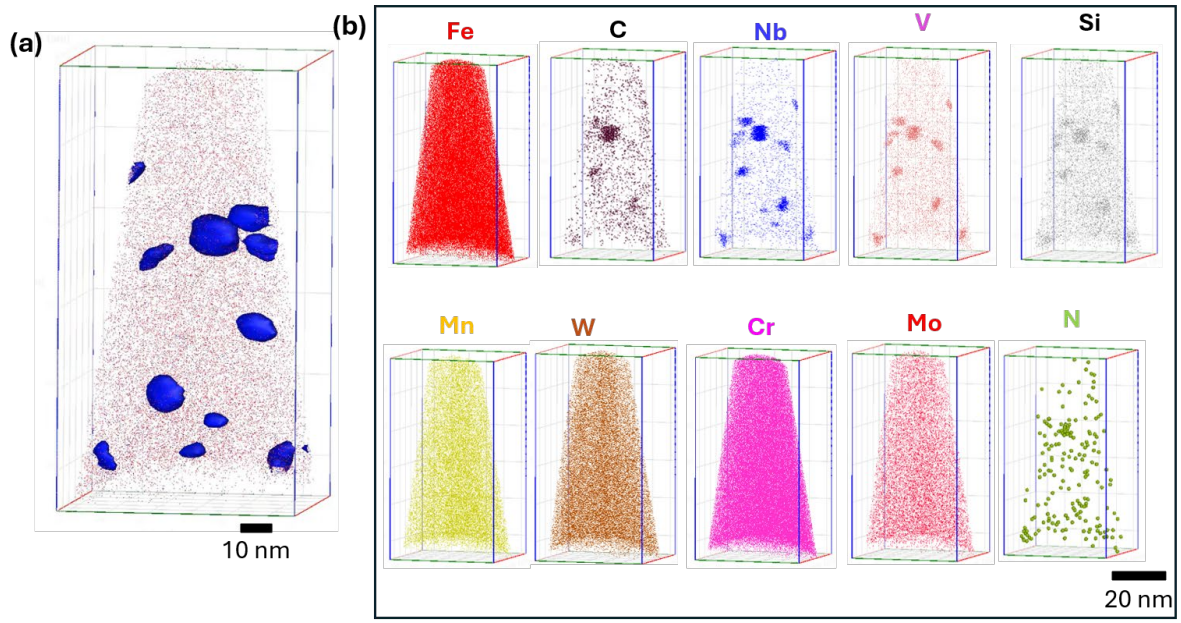


Figure 15. Atom Probe Tomography (APT) Analysis of LP-DED Grade 92 Steel in the Normalized-Plus-Tempered (N+T) Condition. (a) Three-dimensional reconstruction showing iso-concentration surfaces (blue) delineating multiple nanoscale precipitates distributed within the tempered martensitic matrix; scale bar 10 nm. (b) Corresponding elemental atom maps for Fe, C, Nb, V, Si, Mn, W, Cr, Mo, and N extracted from the same volume; scale bar 20 nm.

The three-dimensional reconstruction in Figure 15(a) reveals a population of discrete, approximately equiaxed nanoscale precipitates, typically 5–10 nm in diameter, distributed throughout the analyzed volume with no evidence of preferential alignment or clustering along a single boundary. The elemental maps in Figure 15 (b) identify the chemical nature of these

particles: C, Nb, and V are strongly co-located within the same discrete regions, and Si shows a weaker association with the same features. In contrast, the matrix-forming and substitutional elements Fe, Cr, Mn, W, and Mo are distributed homogeneously across the entire volume. This combination of Nb–V–C co-enrichment in the absence of Cr partitioning identifies the particles as MX-type carbonitrides, which are the principal creep-strengthening dispersion in tempered 9Cr martensitic steels. The homogeneous Cr and W distributions further indicate that the tempering treatment has not produced measurable solute depletion of the matrix at the length scale probed, so the solid-solution strengthening contribution from W and Mo remains intact.

Figure 16 quantifies the composition and interfacial character of these precipitates.

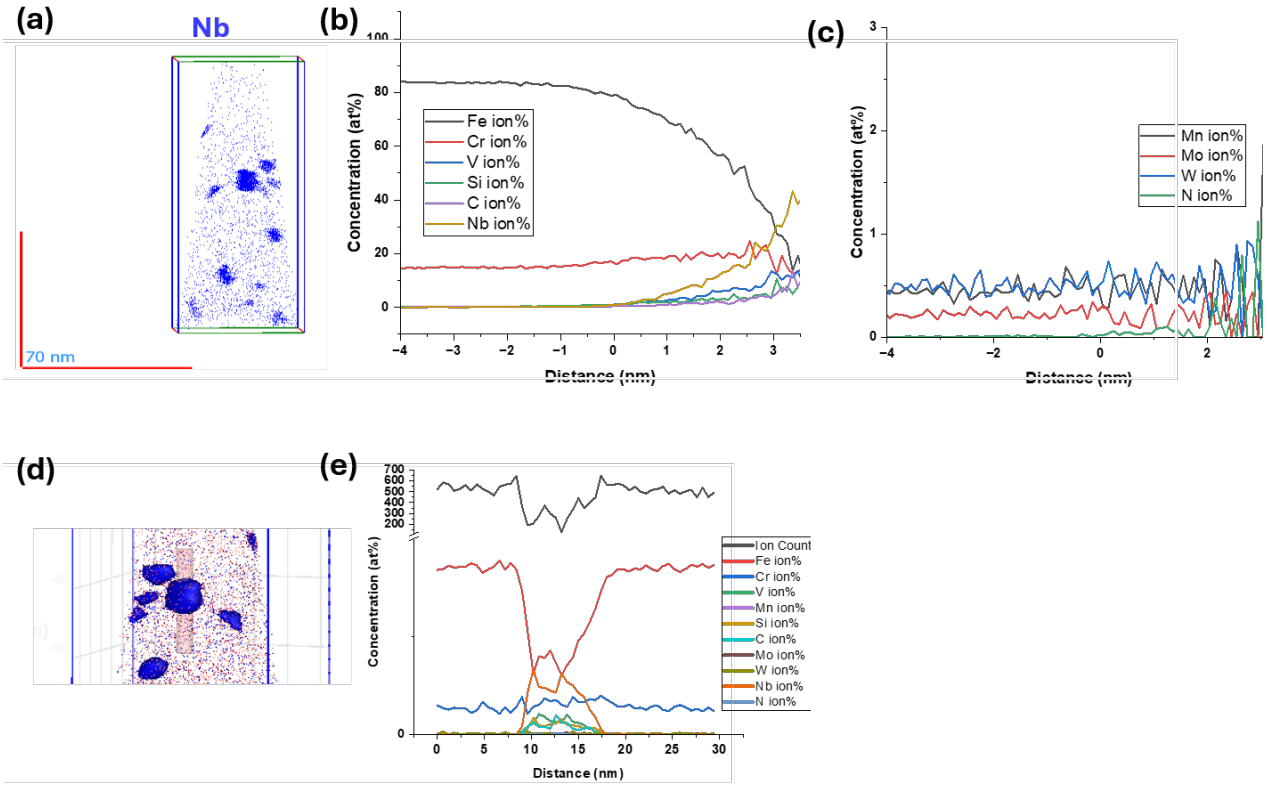


Figure 16. Quantitative APT Analysis Of Precipitates in LP-DED Grade 92 (N+T condition). (a) Nb atom map showing the precipitate distribution within the analyzed volume; scale bar 70 nm. (b, c) Proximity histograms across the precipitate/matrix interface for (b) major species (Fe, Cr, V, Si, C, Nb) and (c) minor species (Mn, Mo, W, N); negative distances correspond to the matrix, positive distances to the precipitate. (d, e) Location and corresponding concentration/ion-count profile of a one-dimensional line scan across a single precipitate.

The Nb atom map in Figure 16(a) confirms that the particles are dispersed uniformly over a length scale of tens of nanometers, consistent with a fine intragranular distribution rather than boundary-decorating carbides. The proximity histograms in Figure 16(b) show a progressive but well-defined compositional transition across the interface: Fe decreases from approximately 82 at.% in the matrix to below 20 at.% within the particle, while Nb, C, V, and Si all increase toward the precipitate interior, with Nb rising most steeply to above 40 at.%. Cr shows only a modest increase and does not dominate the precipitate chemistry, again excluding Cr-rich carbide as the identity of these features. The minor-species profiles in Figure 16 c) indicate that

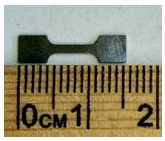
Mn, Mo, W, and N remain at low, near-constant levels through the matrix, with N showing a slight enrichment toward the interface consistent with partial substitution for C on the interstitial sublattice to form a carbonitride rather than a pure carbide. The one-dimensional profile in Figure 16(d, e) confirms this behavior across an individual particle, showing a sharp reciprocal exchange between Fe and Nb over a distance of only a few nanometers.

Taken together, Figure 15 and Figure 16 establish that the N+T treatment applied to LP-DED Grade 92 successfully develops a fine, uniformly distributed population of Nb- and V-rich MX carbonitrides within the tempered martensitic matrix. Such particles are thermodynamically stable and highly resistant to coarsening at 600–650°C and are known to provide effective pinning of dislocations and lath boundaries during creep. Their presence therefore provides a direct microstructural basis for expecting wrought-like creep resistance from the N+T condition and establishes a pre-service baseline against which precipitate coarsening and compositional evolution can be assessed following the planned creep exposures.

4.0 Neutron Irradiation Plan of DED A709

The matrix in Figure 17 has been designed to isolate the combined effects of post-build heat treatment, irradiation temperature, and displacement damage on the mechanical and microstructural response of LP-DED A709. Three microstructural states are included because each presents a fundamentally different starting condition for radiation damage accumulation. The AD condition retains the fine cellular solidification substructure, high dislocation density, and solute segregation characteristic of DED, all of which provide a high density of internal sinks for point defects and may therefore confer intrinsic radiation tolerance. The solution-annealed condition removes this substructure and provides a comparatively clean, low-sink-density austenitic matrix, serving as a reference against which the benefit of the as-built substructure can be quantified. The SA+PT condition contains the Nb-rich MX carbide dispersion identified by atom probe tomography and represents the candidate service microstructure; its behavior under irradiation is critical, since MX particles may act as beneficial defect sinks but are also potentially susceptible to irradiation-induced dissolution, coarsening, or ballistic mixing.

A709-DED Samples **SSJ-2 Samples**



Condition	Temperature	Dose (dpa)	No. of samples
AD	600	2	2
AD	600	10	2
SA	600	2	2
SA	600	10	2
SA+ PT	500	2	2
SA+ PT	500	10	2
SA+ PT	600	2	2
SA+ PT	600	10	2
Total samples			**16**

Figure 17. Neutron Irradiation Matrix for LP-DED-Fabricated A709 Planned at the High-Flux Isotope Reactor, Oak Ridge National Laboratory. SSJ-2 miniature tensile specimens (inset, shown against a centimeter scale) will be irradiated in the as-deposited (AD), solution-annealed (SA), and solution-annealed plus precipitation-treated (SA+PT) conditions at 500 and 600°C to nominal doses of 2 and 10 displacements per atom (dpa), with two specimens per condition for a total of 16 specimens.

Two doses are included to establish the dose dependence of the response. The 2 dpa condition captures the low-dose regime in which defect cluster and dislocation-loop populations develop and hardening typically saturates, while the 10 dpa condition probes the higher-dose regime relevant to extended service, in which void swelling, precipitate instability, and radiation-induced segregation become significant. Comparing the results for the two doses allows saturation

behavior of hardening and the onset of microstructural instability to be distinguished rather than inferred from a single dose. The inclusion of both 500 and 600°C for the SA+PT condition addresses the strong temperature dependence of defect mobility in austenitic steels. The lower temperature favors retention of small defect clusters and greater irradiation hardening, whereas the higher temperature promotes defect recombination and annealing but also accelerates thermally assisted precipitate evolution and cavity nucleation. This pairing therefore identifies whether the candidate microstructure is more vulnerable to hardening-dominated or swelling-dominated degradation across the intended operating window.

Following irradiation, post-irradiation tensile testing of the SSJ-2 specimens will quantify irradiation hardening, loss of strain-hardening capacity, and any reduction in ductility relative to the unirradiated baseline already established in this program. These measurements directly address the principal engineering concerns for structural application, namely irradiation-induced embrittlement and the potential for flow localization. Because the tensile data alone cannot identify the responsible defect populations, complementary transmission electron microscopy will be performed to characterize dislocation-loop densities and size distributions, cavity and void populations, and any changes in precipitate morphology or distribution. Atom probe tomography will then be used to resolve the nanoscale chemistry that TEM cannot access, specifically radiation-induced segregation at grain boundaries and prior-layer interfaces, solute redistribution within the matrix, and the compositional stability of the MX carbides under displacement damage.

The integration of mechanical testing with correlative TEM and APT is essential because the performance of DED A709 in a radiation environment will be determined by whether the process-derived microstructural features that provide its favorable creep and tensile behavior remain stable under irradiation. Establishing these structure–property relationships across a systematic matrix of heat treatments, temperatures, and doses provides the mechanistic basis required for the eventual qualification of additively manufactured A709 for nuclear structural service.

5.0 Discussion

5.1 Role of the As-Deposited Substructure

The mechanical behavior of both LP-DED alloys is governed primarily by the non-equilibrium microstructure inherited from solidification. In A709, the AD condition gave the highest DED strength (AD-H, ~650–850 MPa) while retaining >30% elongation, because the fine cellular substructure, high retained dislocation density and cell-boundary solute segregation provide a distributed obstacle field that impedes dislocation motion without introducing brittle constituents. In Grade 92, the same rapid solidification instead produces untempered martensite, giving exceptional strength (~1,650 MPa) but limited hardening capacity and low elongation (10–16% at RT, 4–5% at 550°C). DED therefore confers strengthening in both systems, but only in the austenitic alloy is it accompanied by useful ductility.

5.2 Effect of Heat Treatment

Heat treatment progressively replaces the metastable deposition substructure with an engineered, stable microstructure. Solution annealing alone gives the lowest strength and highest tensile elongation (40–45%); PT without prior solution treatment raises flow stress but limits elongation to 18-25%; SA+PT provides the most balanced response (30–40% elongation with strength above SA).

The APT results explain this. In the PT condition, discrete Nb- and C-rich MX particles sit within a chemically homogeneous austenite matrix with a sharp 1–2 nm interface, and the absence of residual solute clustering confirms that solution treatment dissolved the deposition-induced segregation. SA+PT thus substitutes a thermodynamically stable precipitate dispersion for the metastable as-built obstacle field. Notably, no Cr depletion is present adjacent to the precipitates, indicating that MX formation does not sensitize the matrix. The same picture holds for Grade 92, where N+T contains a fine dispersion of 5–10 nm Nb- and V-rich MX carbonitrides with homogeneous Cr, W and Mo distributions, the constituents known to control creep life in 9Cr steels.

5.3 Interpretation of the Creep Results

The creep results must be interpreted with caution because a low accumulated strain reflects resistance to creep deformation rather than the capacity to accommodate it, and these properties are not equivalent measures of creep performance. The wrought benchmark ruptured with 48–55% elongation and 50–57% RA, reflecting a microstructure able to accommodate creep strain homogeneously; the property that confers damage tolerance and a deformation-based indication of remaining life.

The AD DED specimens at 650°C/275 MPa remained essentially undeformed beyond 1500 h. This behavior demonstrates a very low minimum creep rate, consistent with the cellular substructure suppressing recovery and dislocation climb. However, these tests are still running and have produced no measurable creep elongation, so **no creep ductility has been demonstrated for the AD condition**. It resists creep deformation but has not shown that it can accommodate creep strain, and the substructure responsible is metastable over service timescales.

The heat-treated conditions have ruptured and can be assessed on ductility. At 650°C/275 MPa, SA failed after 180 h with 9% elongation and 8.6% RA, whereas **SA+PT failed after 350 h with 33% elongation and 30% RA, twice the life and more than three times the ductility of SA**, moving substantially toward wrought-like behavior. This simultaneous improvement in both life and ductility, rather than a trade-off between them, identifies SA+PT as the best-performing LP-DED condition evaluated.

5.4 Mechanistic Basis for the SA+PT Advantage

Three observations confirm that the SA and SA+PT difference reflects a change in failure mechanism rather than strength alone. The SA specimen failed flat and without necking, whereas SA+PT showed clear localized contraction. Fractographically, SA displays faceted, boundary-following features indicative of mixed intergranular fracture, while SA+PT shows a well-developed shear lip and more homogeneously distributed dimples and cavities. Quantitatively, RA rises from 8.6% (SA) to 30% (SA+PT) toward 57% (wrought).

The explanation is that solution annealing removes the intragranular obstacle field without replacing it, concentrating strain at grain and prior-layer boundaries so that cavities nucleate and link before bulk plasticity develops. The $M_{23}C_6$ and MX dispersion introduced by the subsequent precipitation treatment forces deformation back into grain interiors, distributing strain, delaying cavity coalescence and restoring transgranular ductile failure. Therefore, the microscopy and creep ductility results are mutually corroborating.

The pre-creep XCT data show that SA and SA+PT contain comparable porosity, unaffected by heat treatment. Since the defect populations are similar, the large ductility difference must be attributed to the matrix and precipitate state, reinforcing the role of the $M_{23}C_6$ and MX dispersion. These defects nonetheless act as cavity-nucleation sites and explain the off-center creep fractures observed in DED specimens; their removal is the clearest route to closing the remaining ductility gap to wrought material.

5.5 Selection of an Optimum Condition

For **Alloy 709**, SA+PT is the preferred condition. It is the only DED state that has ruptured and demonstrated creep ductility approaching wrought behavior, while doubling the rupture life of SA and possessing a stable, non-sensitizing $M_{23}C_6$ and MX dispersion confirmed by APT. Because it is both shorter-lived and far less ductile than wrought material and fails in a boundary-dominated mode with minimal warning, SA is unsuitable for creep-limited service. Alternatively, AD remains promising, but it is unqualified pending rupture data and a measured elongation.

For **Grade 92**, N appears attractive on tensile evidence (~1250 MPa at 550°C with ~15% elongation and the highest strength retention), but its strength derives from untempered martensite that would temper in service, whereas N+T possesses the coarsening-resistant MX carbonitride dispersion. Given that the Alloy 709 results show a stable intragranular MX dispersion to be the source of creep ductility and life, the planned creep matrix should treat creep elongation and RA as primary discriminators alongside rupture life.

5.6 Implications for the Irradiation Study

The irradiation matrix tests whether these microstructural features remain stable under displacement damage. Because its high internal sink density may promote point-defect recombination, AD is included; SA provides the low-sink-density reference; and SA+PT is the most consequential because it is the preferred service microstructure and its MX carbides may act either as beneficial sinks or as vulnerabilities to irradiation-induced dissolution or coarsening. The two doses separate hardening saturation (2 dpa) from swelling and precipitate instability (10 dpa), while the 500/600°C pair distinguishes hardening-dominated swelling from swelling-dominated degradation. Post-irradiation tensile testing with correlative TEM and APT is essential to understand irradiation-induced segregation and grain boundary-dominated failure seen in SA could re-emerge in SA+PT.

6.0 Conclusions

This report summarizes the tensile, creep, fractographic, and APT characterization of LP-DED fabricated A709 and Grade 92 steels, benchmarked against wrought material, together with the planned creep and neutron-irradiation programs. The principal conclusions are discussed in the following sections.

6.1 Tensile Behavior of LP-DED Alloy 709

The AD condition provided the highest DED strength (AD-H, ~650–850 MPa depending on test temperature), matching or exceeding wrought A709 while retaining fracture strains above 30%. Solution annealing lowered strength but gave the largest elongations (40–45%), whereas precipitation treatment without a prior solution treatment raised flow stress but restricted elongation to 18–25%. The combined SA+PT treatment produced the most balanced response, with strength above SA and 30–40% elongation. Horizontal specimens were consistently stronger than vertical specimens in all conditions, confirming build-orientation anisotropy; this anisotropy was largest AD and was reduced, but not eliminated, by solution annealing. All conditions failed by ductile micro-void coalescence, with isolated pores and lack-of-fusion defects visible on the fracture surfaces.

6.2 Creep Behavior and the Selection of SA+PT

Wrought A709 ruptured with 48–55% elongation and 50–57% RA, establishing a highly ductile, transgranular benchmark. The AD DED specimens accumulated only ~4.5% RA over 1,805 h at 650°C/275 MPa and remained essentially undeformed beyond 1,500 h at 750°C/140 MPa, indicating a very low minimum creep rate; however, these tests remain in progress and have produced no measurable creep elongation, so the creep ductility of the AD condition is unproven. Among the ruptured conditions, SA failed after 180 h with only 9% elongation and 8.6% RA, whereas SA+PT failed after 350 h with 33% elongation and 30% RA. SA+PT therefore doubled the rupture life of SA while tripling its creep ductility and is identified as the best-performing DED condition evaluated. The SA condition is unsuitable for creep-limited service, failing in a boundary-dominated mode with minimal necking and little deformation-based warning.

6.3 Mechanistic Basis

Macroscopic specimen appearance, fractography and reduction-in-area measurements consistently show a progression from boundary-dominated, low-ductility fracture in SA, through mixed-mode fracture in SA+PT, to fully transgranular ductile cavitation in wrought material. Atom probe tomography of the PT condition confirmed discrete Nb- and C-rich MX particles within a chemically homogeneous austenite matrix, with sharp 1–2 nm interfaces and no adjacent Cr depletion, indicating that precipitation does not sensitize the matrix. This intragranular dispersion redistributes strain into grain interiors and delays cavity coalescence at boundaries, providing the direct microstructural explanation for the superior life and ductility of SA+PT.

6.4 Process-Induced Defects

Pre-creep XCT showed that both SA and SA+PT contain comparable porosity distributed along the build direction, unchanged by heat treatment. Because the defect populations are similar, the large ductility difference between the two conditions must be attributed to the precipitate and matrix state. These defects nonetheless explain the off-center creep fractures observed in DED specimens and the residual anisotropy persisting after full heat treatment.

6.5 LP-DED Grade 92

The tensile matrix was completed in FY 2026 with the addition of the N and N+T conditions. The AD material was strongest (~1,650 MPa) but insufficiently ductile, particularly at 550°C where it retained only ~47% of its room-temperature elongation. The N condition showed the highest property retention, while N+T gave the lowest strength but contains the fine coarsening-resistant Nb- and V-rich MX carbonitride dispersion confirmed by APT, the constituent controlling creep life in 9Cr steels. Creep testing against exactly matched wrought benchmarks is required to resolve this, with creep ductility treated as a primary discriminator.

6.6 Outlook

Completion of the ongoing creep tests to rupture, quantitative precipitate statistics, and the planned High Flux Isotope Reactor irradiation of AD, SA and SA+PT specimens at 500–600°C to 2 and 10 dpa are the key steps toward qualifying additively manufactured A709 for nuclear structural service.

7.0 Path Forward

7.1 Completion and Reconciliation of the Existing Dataset

The immediate priority is to close the gaps that currently prevent a full comparison between conditions. The ongoing SA and SA+PT tests at 700°C/160 MPa must be completed to allow direct comparison with the wrought reference at that condition.

Beyond rupture data, the interrupted and ruptured specimens will be examined by post-mortem XCT and by quantitative cavity-density measurements on polished longitudinal sections. This is required to determine whether creep cavities nucleate preferentially at the pre-existing lack-of-fusion defects identified in the pre-creep scans or independently at grain and prior-layer boundaries, a distinction that dictates whether future improvement should target deposition quality or heat-treatment design.

For Grade 91 and Grade 92 steels, the machined specimens will be entered into the planned creep matrix covering AD, N and N+T at both 650°C/140 MPa and 600°C/220 MPa. Creep elongation and RA will be recorded and reported alongside rupture life, since the Alloy 709 results demonstrate that these are the discriminating properties. This dataset is expected to resolve the current conflict between the tensile ranking, which favors the N condition, and the microstructural ranking, which favors N+T.

7.2 Benchmarking Objective

All testing will continue to be benchmarked against wrought material tested under identical temperature–stress conditions rather than against extrapolated or parameterized data. For Alloy 709 steel, this baseline is already established in-house, and for Grade 91/92 steel, the selected literature values of 743 h at 650°C/140 MPa and 475 h at 600°C/220 MPa correspond to conventionally processed normalized-and-tempered material at exactly the planned test conditions.

The benchmarking objective is deliberately twofold. Rupture life establishes whether LP-DED material meets the load-carrying requirement, while creep elongation and RA establish whether it does so with acceptable damage tolerance. On this basis the target is not simply to match wrought rupture life but to demonstrate a condition that combines wrought-equivalent life with wrought-like ductile, transgranular failure. The present results indicate that SA+PT is the closest to this target and should therefore be treated as the reference DED condition against which further process and heat-treatment variants are assessed.

7.3 Microstructure–Thermodynamics Linkage

The APT results have established the identity and chemistry of the strengthening phases in both alloys but not their quantitative dispersion parameters. Additional APT datasets, combined with correlative TEM, will be acquired to extract precipitate number density, mean size, volume fraction and interparticle spacing for the MX populations in SA+PT Alloy 709 and N+T Grade 92 steels. These quantities are the direct inputs required for Orowan and climb-resistance analysis and will allow the observed differences in creep life and creep ductility to be linked quantitatively to the dispersion state rather than inferred from it.

In parallel, computational thermodynamics will be used to predict equilibrium phase fractions at 600–750°C. Comparison of predicted precipitate fraction will indicate how far the heat-treated DED microstructures deviate from equilibrium and will provide an estimate of long-term stability. Post-creep and post-thermal-exposure APT and TEM will be used to verify these predictions directly by tracking precipitate evolution in tested material.

7.4 Irradiation Program

The SSJ-2 specimen set will be irradiated at the High Flux Isotope Reactor in the AD, SA, and SA+PT conditions at 500 and 600°C to nominal doses of 2 and 10 dpa.

8.0 Publications and Presentations

8.1 Publications

- Mahmud, S. Meher, P. Renner, A. Rieffer, C. Silva, J. Snitzer, Q. Zhang, X. Lou, I. Van Rooyen, Optimizing laser powder directed energy deposition for Grade-91 and Grade-92 ferritic/martensitic steels for nuclear applications: linking process parameters to microstructure, Frontiers in Nuclear Engineering Volume 4 - 2025 (2025).

8.2 Conferences

- “Microstructural Optimization, High-Temperature Mechanical Properties, and Ion Irradiation Behavior of DED A709 for Nuclear Applications” S. Meher, A. Mahmud, R. Seffens, M. Rhodes, L. Shao, I. van Rooyen at TMS 2026, San Diego, CA, USA.

- “Microstructure and Mechanical Properties of Heat-Treated Grade-92 Stainless Steels Fabricated by Directed Energy Deposition for Nuclear Applications”, A. Mahmud, S. Meher, X. Lou, J. Snitzer, I. van Rooyen at MINES, 2025, Cleveland, Ohio.

8.3 Milestone Reports

- S. Meher, A. Mahmud, I.J. van Rooyen, Laser Powder Directed Energy Deposition of Steels for Nuclear Applications, Pacific Northwest National Laboratory (PNNL), Richland, WA (United States), United States, 2025
- S. Meher, A. Roy, A. Mahmud, P.A. Renner, C.M. Silva, M.S.K.K.Y. Nartu, A.M. Rieffer, G.A. Valenzuela, I.J. van Rooyen, Studies on Printability Methodologies and Directed-Energy-Deposition-Fabricated Iron Alloys for Nuclear Applications, Pacific Northwest National Laboratory (PNNL), Richland, WA (United States), United States, 2024
- S. Meher, C.M. Silva, M.S.K.K.Y. Nartu, A. Roy, W.E. Frazier, M. Komarasamy, T.A. Ajantiwalay, S. Tripathi, J.B. Wierschke, N.L. Canfield, I.J. van Rooyen, Evaluation of printability methodologies and feasibility to down select LBPF steel and other materials for nuclear applications, United States, 2023.

8.4 AMMT Annual Program Review Meeting Presentations

- High Temperature Tensile and Creep Response of Heat-treated LP-DED Alloys A709 & Gr92, S. Meher, Jens Darsell, J. Lapeyre, F. Sanchez, M. Nartu, I. van Rooyen, June 23, 2026.
- Development and Performance of Additively Manufactured (LPBF & DED) Fe-Based Alloy, S. Meher, A. Mahmud, I. J van Rooyen, July 15, 2026.
- Development of Fe-based Alloys, S. Meher, I. van Rooyen, A. Roy, M. Komarasamy, M. Nartu, P. Renner, A. Mahmud, May 21, 2024.

9.0 References

[1] S. Singh, C. Kumar, S.K. Sah, Review on laser powder-based directed energy deposition for fabricating functionally graded materials: Microstructure, mechanical behavior, and defect analysis, Journal of Laser Applications 37(4) (2025).

[2] S. Chundi, C. Kumar, S. Das, A Comprehensive Review of Current Status, Challenges, and Applications of Laser Powder Directed Energy Deposition (LP-DED) in Metal Additive Manufacturing Process for Inconel and Its Alloys, Lasers in Manufacturing and Materials Processing 13(2) (2026) 621–675.

[3] W. Huang, S. Zhang, Y. Tong, P. Wu, K. Gan, Exceptional creep resistance enabled by thermally stable cellular dislocation structures in an additively manufactured multicomponent alloy, Materials Science and Engineering: A 890 (2024) 145902.

[4] Y. Li, T. Krajňák, P. Podaný, J. Veselý, J. Džugan, Thermal stability of dislocation structure and its effect on creep property in austenitic 316L stainless steel manufactured by directed energy deposition, Materials Science and Engineering: A 873 (2023) 144981.

[5] S. Holdsworth, Creep-Ductility of High Temperature Steels: A Review, Metals 9(3) (2019) 342.

[6] Y. Zhao, M.N. Cinbiz, J.-S. Park, J. Almer, D. Kaoumi, Tensile behavior and microstructural evolution of a Fe-25Ni-20Cr austenitic stainless steel (alloy 709) from room to elevated temperatures through in-situ synchrotron X-ray diffraction characterization and transmission electron microscopy, Journal of Nuclear Materials 540 (2020) 152367.

[7] T.-L. Sham, R.E. Bass, Y. Wang, X. Zhang, A709 Qualification Plan Update and Mechanical Properties Data Assessment, United States, 2022, p. Medium: ED.

[8] Y. Wang, X. Fan, Summary of FY 2024 A709 Code Case testing at ANL, INL and ORNL, Oak Ridge National Laboratory (ORNL), Oak Ridge, TN (United States), United States, 2024, p. 28 p.

[9] N. Mohale, R.E. Bass, Microstructural Characterization of A709 Commercial Heats with Precipitation Treatment, Idaho National Laboratory (INL), Idaho Falls, ID (United States), United States, 2022.

[10] X. Zhang, E.J. Listwan, FY25 Status Update on A709 Code Case Testing at ANL, Argonne National Laboratory (ANL), Argonne, IL (United States), United States, 2025, p. 22 p.

[11] R.L. Klueh, A.T. Nelson, Ferritic/martensitic steels for next-generation reactors, Journal of Nuclear Materials 371(1) (2007) 37–52.

[12] S. Meher, A. Mahmud, I.J. van Rooyen, Laser Powder Directed Energy Deposition of Steels for Nuclear Applications, Pacific Northwest National Laboratory (PNNL), Richland, WA (United States), United States, 2025.

[13] E.R. Proehl, W. Zhong, D.J. Sprouster, C.R. Lear, M.M. Schneider, C.M. Parish, B.P. Eftink, L.L. Snead, S.J. Zinkle, L. Tan, Effect of stress on Laves phase precipitation in creep ruptured Grade 92 ferritic martensitic steel characterized by a novel accessible method, Acta Materialia 301 (2025) 121559.

[14] L. Tan, Assessment of the propensity of low creep ductility for optimized Grade 92 steel, Oak Ridge National Laboratory (ORNL), Oak Ridge, TN (United States), United States, 2018.

Pacific Northwest National Laboratory

902 Battelle Boulevard
P.O. Box 999
Richland, WA 99354

1-888-375-PNNL (7665)

www.pnnl.gov